

# The hyperplane of early-type galaxies: using stellar population properties to increase the precision and accuracy of the fundamental plane as a distance indicator

Francesco D'Eugenio <sup>1,2,3\*</sup>, Matthew Colless <sup>4,5</sup>, Arjen van der Wel <sup>3</sup>, Sam P. Vaughan <sup>6,5</sup>, Khaled Said <sup>7</sup>, Jesse van de Sande <sup>6,5</sup>, Joss Bland-Hawthorn <sup>6,5</sup>, Julia J. Bryant <sup>6,8,5</sup>, Scott M. Croom <sup>6,5</sup>, Ángel R. López-Sánchez <sup>9,10,5</sup>, Nuria P. F. Lorente <sup>11</sup>, Roberto Maiolino <sup>1,2,12</sup> and Edward N. Taylor <sup>13</sup>

<sup>1</sup>Kavli Institute for Cosmology, University of Cambridge, Madingley Road, Cambridge, CB3 0HA, United Kingdom

<sup>2</sup>Cavendish Laboratory - Astrophysics Group, University of Cambridge, 19 JJ Thomson Avenue, Cambridge, CB3 0HE, United Kingdom

<sup>3</sup>Sterrenkundig Observatorium, Universiteit Gent, Krijgslaan 281 S9, B-9000 Gent, Belgium

<sup>4</sup>Research School of Astronomy and Astrophysics, Australian National University, Canberra, ACT 2611, Australia

<sup>5</sup>ARC Centre of Excellence for All Sky Astrophysics in 3 Dimensions (ASTRO 3D), Australia

<sup>6</sup>Sydney Institute for Astronomy, School of Physics, The University of Sydney, NSW, 2006, Australia

<sup>7</sup>School of Mathematics and Physics, The University of Queensland, Brisbane, QLD 4072, Australia

<sup>8</sup>Australian Astronomical Optics, Astralis-USydney, School of Physics, University of Sydney, NSW 2006, Australia

<sup>9</sup>School of Mathematical and Physical Sciences, Macquarie University, NSW 2109, Australia

<sup>10</sup>Macquarie University Research Centre for Astrophysics and Space Technologies, NSW 2109, Australia

<sup>11</sup>AAO-MQ, Faculty of Science & Engineering, Macquarie University, 105 Delhi Rd, North Ryde, NSW 2113, Australia

<sup>12</sup>Department of Physics and Astronomy, University College London, Gower Street, London WC1E 6BT, UK

<sup>13</sup>Centre for Astrophysics and Supercomputing, Swinburne University of Technology, Hawthorn, VIC 3122, Australia

Accepted 2024 June 21. Received 2024 May 30; in original form 2023 July 19

## ABSTRACT

We use deep spectroscopy from the SAMI Galaxy Survey to explore the precision of the fundamental plane of early-type galaxies (FP) as a distance indicator for future single-fibre spectroscopy surveys. We study the optimal trade-off between sample size and signal-to-noise ratio (SNR), and investigate which additional observables can be used to construct hyperplanes with smaller intrinsic scatter than the FP. We add increasing levels of random noise (parametrised as effective exposure time) to the SAMI spectra to study the effect of increasing measurement uncertainties on the FP- and hyperplane-inferred distances. We find that, using direct-fit methods, the values of the FP and hyperplane best-fit coefficients depend on the spectral SNR, and reach asymptotic values for a mean  $\langle SNR \rangle = 40 \text{ \AA}^{-1}$ . As additional variables for the FP we consider three stellar-population observables: light-weighted age, stellar mass-to-light ratio and a novel combination of Lick indices ( $I_{\text{age}}$ ). For a  $\langle SNR \rangle = 45 \text{ \AA}^{-1}$  (equivalent to 1-hour exposure on a 4-m telescope), all three hyperplanes outperform the FP as distance indicators. Being an empirical spectral index,  $I_{\text{age}}$  avoids the model-dependent uncertainties and bias underlying age and mass-to-light ratio measurements, yet yields a 10 per cent reduction of the median distance uncertainty compared to the FP. We also find that, as a by-product, the  $I_{\text{age}}$  hyperplane removes most of the reported environment bias of the FP. After accounting for the different signal-to-noise ratio, these conclusions also apply to a 50 times larger sample from SDSS-III. However, in this case, only *age* removes the environment bias.

**Key words:** cosmology: distance scale – galaxies: distances and redshifts – galaxies: fundamental parameters – galaxies: structure

\* E-mail: francesco.deugenio@gmail.com

## 1 INTRODUCTION

The ‘fundamental plane’ is an empirical multilinear relation between three galaxy observables: size, velocity dispersion, and surface brightness (FP; Djorgovski & Davis 1987; Dressler et al. 1987). The relation deserved the name ‘plane’ because of its remarkable tightness (root mean square  $rms \approx 0.1$  dex) relative to the range of the three observables, which span  $\approx 0.5$ – $1$  dex. Nevertheless, the FP is known to be warped (e.g., Yoon & Park 2022) and does not extend into the domain of dwarf galaxies (Eftekhari et al. 2022). Moreover, the FP has non-zero intrinsic scatter ( $\sigma_{\text{intr}}$ ; Jørgensen et al. 1996, Hyde & Bernardi 2009, Magoulas et al. 2012; hereafter: M12).

Because the FP can express distance-dependent size as a function of distance-independent velocity dispersion and surface brightness, it can be used as a distance indicator (e.g. Hudson et al. 1997, 1999; Colless et al. 2001). Initially, the limiting factor of FP-derived distances were the precision of the measured galaxy observables and small sample sizes. However, the next generation of surveys was able to obtain more precise measurements for larger samples (e.g., 6dFGS, the 6-degree Field Galaxy Survey, Jones et al. 2004; and SDSS, the Sloan Digital Sky Survey, York et al. 2000). For this new generation of surveys—and for every FP survey since—FP cosmology was limited by the plane’s  $\sigma_{\text{intr}}$  (M12, Johnson et al. 2014, Said et al. 2020). This is a physical boundary that cannot be overcome by increasing the size of the sample, but requires understanding the physical drivers of  $\sigma_{\text{intr}}$ , be it new models (e.g., non-linear formulations of the ‘FP’) or new observables (e.g., a higher-dimensional ‘FP’).

Several studies have attempted to ‘explain’  $\sigma_{\text{intr}}$ ; that is, to find the physical origin of this scatter. The underlying hypothesis is that the FP is rooted in the virial theorem, which links size and velocity dispersion to dynamical mass (e.g. Faber et al. 1987; Dressler et al. 1987). Going from the virial theorem to the FP means going from unobservable dynamical mass to luminosity, which we can measure. This requires adding various terms that depend on the structure and content of galaxies, but that can be expressed as functions of the FP observables (e.g. Prugniel & Simien 1996, 1997; Graves et al. 2009). Unlike the virial theorem, these additional terms are expected to possess some intrinsic scatter, due, e.g., to differences in the structure, mass distribution and stellar-population content of galaxies, and it is in this physical scatter that the FP  $\sigma_{\text{intr}}$  likely originates. There is an extensive literature concerning the physical origin of  $\sigma_{\text{intr}}$ , with various works pointing to trends in the stellar-population properties (Gregg 1992; Prugniel & Simien 1996; Forbes et al. 1998; Graves et al. 2009; Falcón-Barroso et al. 2011; Springob et al. 2012; Yoon & Park 2020), including variations in the initial mass function (IMF; Graves & Faber 2010), dark matter fraction (Zaritsky et al. 2006), or structural variations (Prugniel & Simien 1997).

The advent of extensive integral-field spectroscopy (IFS) surveys, with their large collecting areas, has enabled observations of unprecedented depth for statistical samples. Using a mass- and volume-limited sample from the SAMI Galaxy Survey (Croom et al. 2012), D’Eugenio et al. (2021, hereafter: DE21) have shown that the residuals of the FP have the largest magnitude and most significant correlation with stellar population age; in particular, at any fixed posi-

tion on the FP, the oldest/youngest galaxies lie on average below/above the plane. Regardless of the physical interpretation of this result, this suggests that age could be added to the FP as a fourth observable to remove the age bias and reduce  $\sigma_{\text{intr}}$ . While the problem of removing the age bias has already been addressed (e.g., Guzman & Lucey 1993), improving the FP precision has proven more challenging. Previous attempts were unsuccessful because the additional observational scatter due to low-precision age measurements is greater than the prospective reduction in  $\sigma_{\text{intr}}$ , producing an overall *degradation* of the FP precision (M12). However, the quality of synthetic-aperture spectra from IFS surveys is much better than that of even the best single-fibre surveys, enabling us to explore the regime where age (or any other suitable observable) might be sufficiently precisely determined to overcome both measurement uncertainties and intrinsic scatter in the distance estimates.

Interestingly, and apparently unrelated, recent results using SDSS data suggest that the FP suffers from environment bias, such that galaxies in rich/sparse environments lie systematically below/above the plane (Howlett et al. 2022; hereafter: H22). This could be a problem for near-field cosmology applications of the FP, although the trend with environment was found to be weak in DE21. We note, however, that age is known to correlate strongly with environment density, so that the age and environment correlations with the FP residuals are likely related.

Any proposed reduction of  $\sigma_{\text{intr}}$ , to be advantageous to cosmology, must balance the requirement of higher data quality with sample size. For a survey of fixed total duration, longer exposure times (required to lower  $\sigma_{\text{intr}}$ ) come directly at the expense of smaller sample size (which increases the distance uncertainty). It is therefore reasonable to expect that there is an optimal exposure time that minimises the *total* distance uncertainty.

The goal of this work is twofold. First, we propose to realise the promise of a more precise FP by folding in stellar population information of adequate precision; this will in turn increase the accuracy of FP-derived distances, by reducing the magnitude and significance of the residual correlation with environment. Second, we also propose to find the optimal exposure time that a survey must adopt to maximise the efficiency of the allocated total time.

The paper is structured as follows. In § 2 we introduce the SAMI Galaxy Survey, the measurements and the sample selection. We then compare the FP to three alternative ‘hyperplanes’, which add a stellar population age-related observable as a fourth parameter (§ 3). We then discuss the implications of our findings for future FP surveys (§ 6) and conclude with a summary of our findings (§ 7).

Throughout this work, we assume a flat  $\Lambda$ CDM cosmology with  $H_0 = 70 \text{ km s}^{-1} \text{ Mpc}^{-1}$  and  $\Omega_m = 0.3$ . All magnitudes are in the AB system (Oke & Gunn 1983) and, unless otherwise specified, stellar masses and mass-to-light ratios assume a Chabrier IMF (Chabrier 2003).

## 2 DATA AND SAMPLE

The SAMI Galaxy Survey provides an unsurpassed combination of high signal-to-noise ratio, large sample size and, crucially, a broad range of environments, from isolated galaxies

to dense galaxy clusters. The first goal of this section is to present the data, referring the reader to the relevant literature for a thorough description of the data reduction and verification (§ 2.1). The goal of this paper is to use the superior quality of our IFS observations to study the effect of data quality on the precision of FP-derived distances from single-fibre surveys. In § 2.2 we describe the procedure we used to degrade the data quality, i.e. to simulate observations with exposure times shorter than the actual exposure time of SAMI. We then use these simulated observations to measure aperture velocity dispersions (§ 2.4), stellar population ages (§ 2.5) and a new empirical index  $I_{\text{age}}$  (§ 2.6). In § 2.8 we describe the sample selection criteria and, finally, we illustrate the methods used to derive the best-fit parameters of the 4-d hyperplane (§ 2.9).

## 2.1 The SAMI Galaxy Survey

The SAMI Galaxy Survey (hereafter simply SAMI) is the Australian state-of-the-art integral-field-spectroscopy extragalactic survey (Croom et al. 2012). SAMI used the Sydney-AAO Multi-object Integral field spectroscopy instrument (hereafter: the SAMI instrument), formerly mounted at the prime focus of the 4-metre Anglo-Australian Telescope. The SAMI instrument is endowed with 13 independent integral field units (IFUs), deployable anywhere inside a circular field of view of diameter 1 degree. Each IFU consists of 61 fused fibres of 1.6-arcsec diameter (hexabundles; Bland-Hawthorn et al. 2011; Bryant et al. 2014): compared to ordinary fibre bundles, hexabundles are more fragile, but have 50 per cent-larger fill factor (Croom et al. 2012).

The 13 IFUs, alongside 26 individual sky fibres, are plugged into a pre-drilled metal plate, and are held in position using magnetic connectors. The fibres feed the double-beam AAOmega spectrograph (Sharp et al. 2006), configured with the 570V grating at 3750–5750 Å (blue arm) and the R1000 grating at 6300–7400 Å (red arm). The spectral resolution of the blue arm is  $R = 1812$  ( $\sigma = 70.3 \text{ km s}^{-1}$ ), whereas for the red arm it is  $R = 4263$  ( $\sigma = 29.9 \text{ km s}^{-1}$ ; van de Sande et al. 2017). Each plate is observed for approximately 3.5 hours, using seven dithered observations arranged in a hexagonal pattern (Sharp et al. 2015). The median full-width-at-half-maximum (FWHM) seeing is 2.06 arcsec, with a standard deviation of 0.40 arcsec. We use data available as part of the third public data release (DR3; Croom et al. 2021). The data reduction is originally described in Sharp et al. (2015) and Allen et al. (2015), with a number of improvements explained in the subsequent public data release papers (Green et al. 2018; Scott et al. 2018; Croom et al. 2021).

To match spectroscopy from the SDSS-I and II surveys, we use 1-d spectra from the synthetic circular apertures of radius 1.5 arcsec<sup>1</sup>, which are available in the public SAMI database. The spectra from the blue and red arms of the spectrograph are combined into a single spectrum of uniform spectral resolution (van de Sande et al. 2017).

<sup>1</sup> Note this is different from the SDSS-III spectra, which used the BOSS spectrograph and fibres of 1-arcsec radius. However, the BOSS sample is not appropriate for near-field FP cosmology and is not used here.

## 2.2 Degrading the SAMI spectra

The long exposure times of SAMI ensure a higher signal-to-noise ratio (SNR) than that of typical single-fibre surveys (for our sample, we have a median rest-frame  $g$ -band SNR of  $86.7 \text{ \AA}^{-1}$ , whereas the sample from H22 has  $24.2 \text{ \AA}^{-1}$ ). However, this superior data quality comes at the price of sample size, which for SAMI is smaller by an order of magnitude. While we can reasonably predict that increasing the sample size by a factor  $N$  would decrease the uncertainty of the FP parameters by  $\sqrt{N}$ , understanding the effect of data quality on the uncertainty of age measurements is much more challenging, due to the non-linear nature of the measurement. For this reason, we propose to simulate the effect of *shorter* exposure times on the quality of the SAMI spectra. To do so, we need first a robust estimate of the actual SNR, which we obtain from the residuals of the best-fit spectrum. We fit the SAMI aperture spectra with the MILES stellar template library (Sánchez-Blázquez et al. 2006), using PPF (penalised PiXel Fitting, Cappellari & Emsellem 2004; Cappellari 2017, 2022) and assuming a Gaussian line-of-sight velocity distribution (LOSVD). Following van de Sande et al. (2017), we use a 12<sup>th</sup>-order additive Legendre polynomial. We mask both strong sky lines and regions that are subject to strong emission lines from the gas. For SAMI, the instrument spectral resolution is uniform (full-width half-maximum (FWHM) of  $2.65 \text{ \AA}$ , van de Sande et al. 2017); for the MILES library, we use a uniform FWHM of  $2.51 \text{ \AA}$  (Falcón-Barroso et al. 2011). For most galaxies, SAMI spectral resolution is coarser than the MILES value, so we match the two by broadening the templates with the appropriate kernel. However, for 240 galaxies with redshift  $z > 0.0558$ , the rest-frame spectral resolution of SAMI is better than  $2.51 \text{ \AA}$ , so, in principle, we should degrade the data to match the templates. To avoid this, we take no action, which introduces a bias in the FWHM of up to 4 per cent for the magnitude-limited sample, at the maximum redshift  $z = 0.0997$ . However, the effect on the measured kinematics is smaller than 4 per cent, because our sample has even higher physical dispersion (the 1<sup>st</sup> percentile is  $77 \text{ km s}^{-1}$ ), and because, to first order, the instrument spectral resolution is subtracted in quadrature from the observed broadening.

From the residuals of the best-fit spectrum, we estimate the noise spectrum as follows. First, we calculate the bi-weight scale of the residuals in a moving window of  $54 \text{ \AA}$  (this is a robust estimate of the standard deviation). Masked pixels are not considered in the estimate. Afterwards, the noise vector  $n_{\text{SAMI}}(\lambda)$  is linearly interpolated over missing pixels. The resulting ‘true’ signal-to-noise ratio,  $\text{SNR}_{\text{SAMI}}(\lambda)$ , is defined as the ratio between the spectrum and  $n_{\text{SAMI}}(\lambda)$ . To simulate the spectrum from an exposure of duration  $t_{\text{exp}}$ , we need to define a noise spectrum from which to draw random noise, then add this noise to the original SAMI spectrum. We first calculate the ratio  $f_{\text{exp}}$  between  $t_{\text{exp}}$  and the true exposure time  $t_{\text{SAMI}}$ ; we then estimate the resulting  $\text{SNR}(\lambda)$  as  $\sqrt{f_{\text{exp}}} \text{SNR}_{\text{SAMI}}(\lambda)$ . The additional noise required to go from  $\text{SNR}_{\text{SAMI}}(\lambda)$  to the target SNR is equal to

$$n_{\text{SAMI}}(\lambda) \sqrt{\left(\frac{\text{SNR}_{\text{SAMI}}(\lambda)}{\text{SNR}(\lambda)}\right)^2 - 1}. \quad (1)$$

For each pixel, we draw randomly from the Gaussian distri-

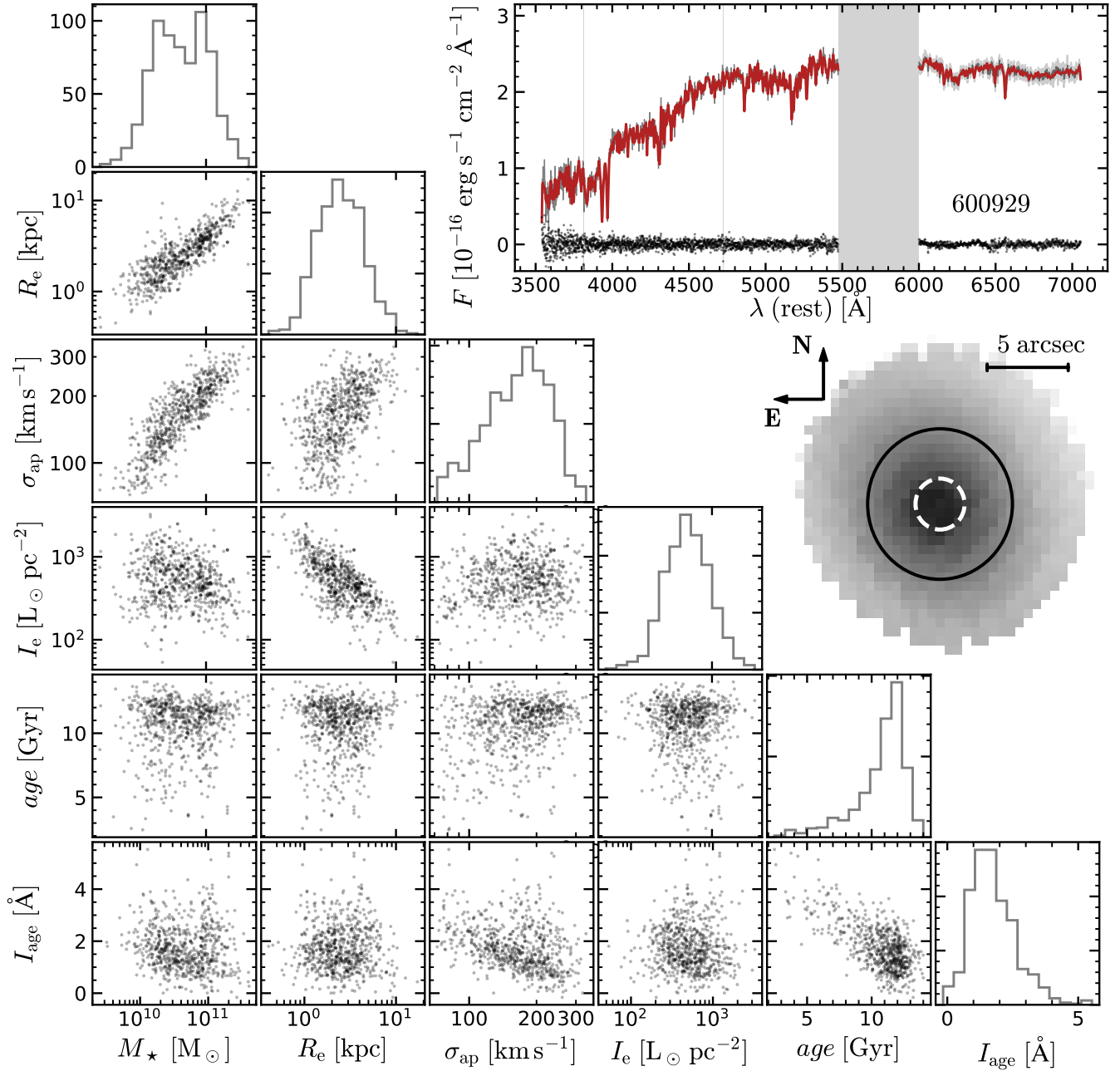


**Figure 1.** The properties of our sample of early-type galaxies, selected to mimic the SDSS sample of Said et al. (2020). Note, in particular, the tail of galaxies with stellar population ages of 3–7 Gyr. These galaxies greatly increase the scatter of the FP (see Fig. 8a), but they cannot be rejected by selection on the H $\alpha$  equivalent width. Besides, rejecting young early-type galaxies introduces a bias with environment, due to the link between local environmental density and stellar-population age (see Fig. 12). The  $I_{age}$  spectral index, an empirical proxy for the FP residuals, is defined in § 2.6. The inset image is the synthetic IFU-derived image of galaxy 600929, which we randomly selected from the sample; the dashed white circle has a radius of 1.5 arcsec and denotes the synthetic aperture we used for our spectroscopy, while the solid black circle shows the half-light radius,  $R_e$  (4.1 arcsec). The top-right panel shows the spectrum within the 1.5-arcsec radius for the same galaxy; the black line is the data, the grey region above/below the data is the 1- $\sigma$  uncertainty, the red line is the PXP best-fit spectrum and the dots are the residuals (the vertical grey bands are not fit).

bution with the corresponding noise, and add the result to the SAMI spectrum. The SAMI noise vector is updated by adding in quadrature the additional noise.

For each galaxy in SAMI, we repeat this procedure for the following exposure times: 0.125, 0.1875, 0.25, 0.375, 0.5, 0.75, 1, 1.5, 2, and 3 hours, thus creating a set of ten mock surveys. These exposure times are related by factors of 2

from 2 hours and 3 hours. Note that whenever  $t_{exp} = t_{SAMI}$ , no noise is added. Moreover, whenever  $t_{exp} > t_{SAMI}$ , that galaxy is excluded from the mock survey; in practice, this happens only for the mocks with  $t_{exp} = 3$  hours, because only 266 galaxies have  $t_{SAMI} < 3$  hours (8 per cent), and none have  $t_{SAMI} < 2$  hours.

After creating these mock observations, we measure

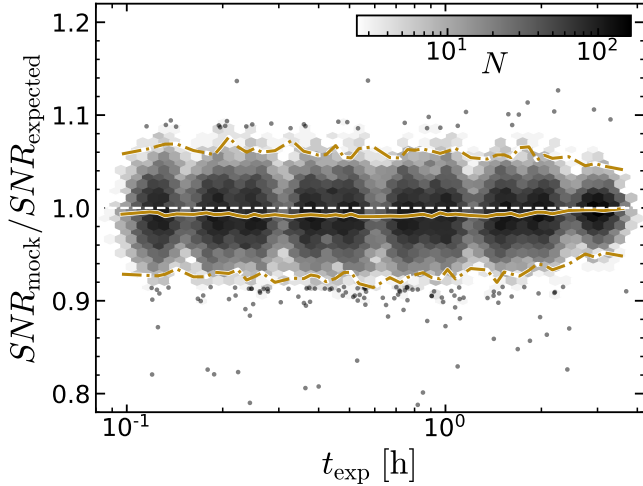


**Figure 2.** Ratio between the measured and expected SNR for all mock spectra, as a function of the mock exposure time; more than 99 per cent of the ratios are within 10 per cent. The expected SNR is given by the true SNR of the SAMI spectra, multiplied by the square root of the ratio between the mock exposure time and the SAMI exposure time; the measured SNR is the standard deviation of the residuals from the best-fit PPF spectrum to the mock spectrum. The white dashed line traces unity (the value expected from a self-consistent noise model); the solid and dot-dashed lines trace respectively the median, and the 1<sup>st</sup>–99<sup>th</sup> percentiles of the mocks. Bins represent regions with more than two mocks; individual mocks are represented by black dots. Note that there are only ten exposure times, but we randomly perturbed these discretised values by 10 per cent for display purposes.

their empirical SNR and, as a sanity check, we verify that it falls close to the expected SNR. In Fig. 2, we compare the empirical SNR measured from the degraded mock spectrum to the SNR expected given the original SNR and exposure time. The ratios are shown as a function of  $t_{\text{exp}}$ , for each of the ten mocks (for display purposes, the exposure times of individual mock spectra have been randomly perturbed by 10 per cent). The ratio of SNRs are normalised by the square root of the ratio of the exposure times, so the values should be close to unity (white dashed line in Fig. 2). Indeed, only 0.2 per cent of the mocks have a SNRs ratio more than 10 per cent from unity, only 0.03 per cent have discrepancy more than 20 per cent from unity, and none lie beyond 30 per cent from unity. There is a bias in that the mocks’ SNR is lower than the expected value, with the median ratio equal to 0.993 (solid line in Fig. 2). In practice, this bias is negligible compared to real effects that we do not model, e.g., the fact that at some point, noise due to sky subtraction residuals or even read-out noise may become dominant over photon noise, invalidating our assumed scaling of the SNR with the square root of the exposure time. We conclude that the SNR estimates and the degrading pipeline work as expected.

### 2.3 Sample SNR vs exposure time

A key validation of our mock data is the relation between  $t_{\text{exp}}$  and  $\langle \text{SNR} \rangle$ . To each value of  $t_{\text{exp}}$ , we associate  $\langle \text{SNR} \rangle$ , the rest-frame  $g$ -band empirical SNR in units of rest-frame  $\text{\AA}^{-1}$ , calculated as the median over the whole sample of

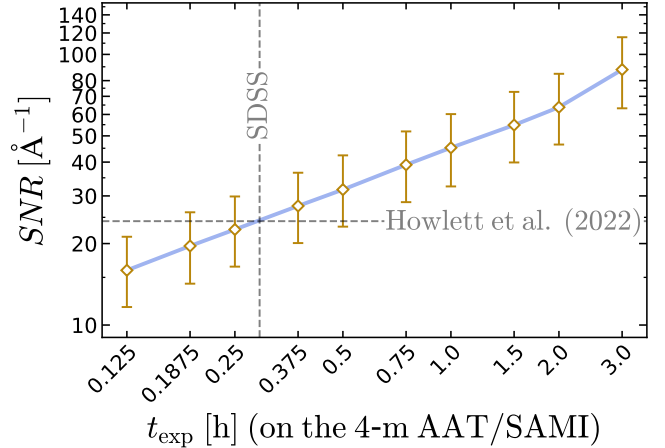


**Figure 3.** Median sample  $g$ -band SNR versus mock exposure time. The errorbars mark the 16<sup>th</sup>–84<sup>th</sup> percentiles of the SNR distribution for each mock; the dashed lines are the exposure time of SDSS (rescaled to AAT/SAMI) and the median SNR of the SDSS sample from H22; interpolating between the mocks we predict SDSS to have a median SNR very close to the experimental value.

703 galaxies. The results are shown in Fig. 3, where for each of the ten mocks the diamonds represent  $\langle \text{SNR} \rangle$  and the errorbars encompass the 16<sup>th</sup>–84<sup>th</sup> percentiles of the SNR distribution. As a benchmark, we report the equivalent exposure time of SDSS spectroscopy ( $t_{\text{SDSS}}$ , vertical dashed line). We assume the total throughput of SDSS and AAT/SAMI to be comparable, so we estimate  $t_{\text{SDSS}}$  on AAT/SAMI by rescaling the true SDSS exposure time of 0.75 hours by the ratio of the telescope areas and get  $t_{\text{SDSS}} = 0.3$  hours. We already reported that the  $g$ -band  $\langle \text{SNR} \rangle$  of the SDSS sample from H22 is  $24.2 \text{ \AA}^{-1}$  (horizontal dashed line in Fig. 3; see also § 5). As an independent validation of our mocks, the solid blue line (which simply connects the diamonds to guide the eye) passes very close to where the dashed lines  $t_{\text{exp}} = 0.3$  hours and  $\langle \text{SNR} \rangle = 24.2 \text{ \AA}^{-1}$  intersect. Interpolating linearly between the mocks with  $t_{\text{exp}} = 0.25$  and 0.375 hours, which have  $\langle \text{SNR} \rangle$  of  $22.5$  and  $27.5 \text{ \AA}^{-1}$ , we find that for  $t_{\text{SDSS}}$  we would obtain  $\langle \text{SNR} \rangle = 25.5 \text{ \AA}^{-1}$ , only 5 per cent larger than the experimental value.

### 2.4 Aperture velocity dispersions

Aperture velocity dispersions  $\sigma_{\text{ap}}$  are measured with the same algorithm we applied to get the best fit used in the SNR estimate. The data are validated by comparing these measurements to the corresponding measurements from DE21. We find

$$\log \sigma_{\text{ap}} = (0.962 \pm 0.004) \log \sigma_{\text{ap,DE21}} + (0.086 \pm 0.009) \quad (2)$$

with a scatter of 0.016 dex, fully explained by measurement uncertainties (see below). To estimate the measurement uncertainties, we use repeat observations. We have overall 165 galaxies with two observations, 62 with three observations, and 21 galaxies with four observations. These can be arranged in 477 possible pairs, of which we consider only 352 independent pairs. Considering together all ten mock samples, we have 3520 pairs of spectra. We reject 330 pairs where the SNRs differ by more than 50 per cent (using a stricter

cut of 10 per cent removes 2073 pairs, but does not change our results, as described below). To estimate the relative uncertainties, we calculate the natural logarithm of the ratio between each pair of  $\sigma_{\text{ap}}$  measurements, then take the bi-weight scale of the logarithm of the ratio in twenty-one bins in SNR (changing the number of bins does not change the final estimated uncertainties). The result is shown by the golden circles in Fig. 4a. We fit these twenty-one values and find that the uncertainty about  $\sigma_{\text{ap}}$  can be expressed as

$$\frac{u(\sigma_{\text{ap}})}{\sigma_{\text{ap}}} = (0.09 \pm 0.01)^2 + \left( \frac{\text{SNR} [\text{\AA}^{-1}]}{5.7 \pm 0.3} \right)^{-(1.86 \pm 0.12)} \quad (3)$$

(solid golden line in Fig. 4a). The uncertainties about the best-fit parameters of Eq. (3) are estimated by bootstrapping the sample of 352 pairs of measurements one thousand times, then taking the biweight scale of the distribution of each of the three parameters. If we were to reject all pairs where the two SNRs differ by more than 10 per cent, we would find the same result, as highlighted by the blue diamonds in Fig. 4a; in particular, the best-fit parameters of Eq. (3) would be  $0.08 \pm 0.02$ ,  $5.1 \pm 0.4$  and  $-1.76 \pm 0.11$  (dashed blue line in Fig. 4a). From here on, the uncertainties on  $\sigma_{\text{ap}}$  are estimated using Eq. (3).

## 2.5 Light-weighted stellar population ages

We use light-weighted stellar-population age from full spectral fitting (FSF), obtained again from PPXF. As input spectra, we use the MILES simple stellar population (SSP) library (Vazdekis et al. 2010, 2015), with BaSTI isochrones (Pietrinferni et al. 2004, 2006) and solar abundance. The age-metallicity grid consists of 53 age bins spanning  $0.03 \text{ Gyr} < \text{SSP age} < 14 \text{ Gyr}$  and 12 metallicity bins spanning  $-2.27 < [Z/H] < 0.4$ . To match the spectral resolution of this library to the SAMI data, we use the same procedure adopted in § 2.2, because the MILES SSP has the same spectral resolution as the MILES stellar template library used in § 2.2. This time, we use multiplicative Legendre polynomials, following Owers et al. (2019). No regularisation is applied because we prioritise goodness of fit over realistic star-formation histories. The light-weighted stellar population age is averaged in log-space (McDermid et al. 2015). From here on, we refer to these ages measurements in italics (*age*); when we want to refer to age in general, we use normal font ‘age’.

The uncertainties on *age* are estimated as for  $\sigma_{\text{ap}}$ , by comparing repeat observations. Fig. 4b shows the value of the uncertainty on *age* as a function of SNR; the symbols have the same meaning as for  $\sigma_{\text{ap}}$  (§ 2.5). For individual spectra of a given SNR, we calculate the relative uncertainty on *age*

$$\frac{u(\textit{age})}{\textit{age}} = (0.13 \pm 0.08)^2 + \left( \frac{\text{SNR} [\text{\AA}^{-1}]}{4.3 \pm 0.3} \right)^{-(1.02 \pm 0.07)} \quad (4)$$

(solid golden line in Fig. 4b). Using the stricter cut at 10 per cent, we would get somewhat smaller uncertainties (up to 20 per cent smaller at the high-SNR end, cf. the solid golden and dashed blue lines in Fig. 4b). In this case, the best-fit relation describing the uncertainties has parameters:  $0.12 \pm 0.07$ ,  $4.3 \pm 0.2$  and  $-1.05 \pm 0.07$ ; as can be seen,

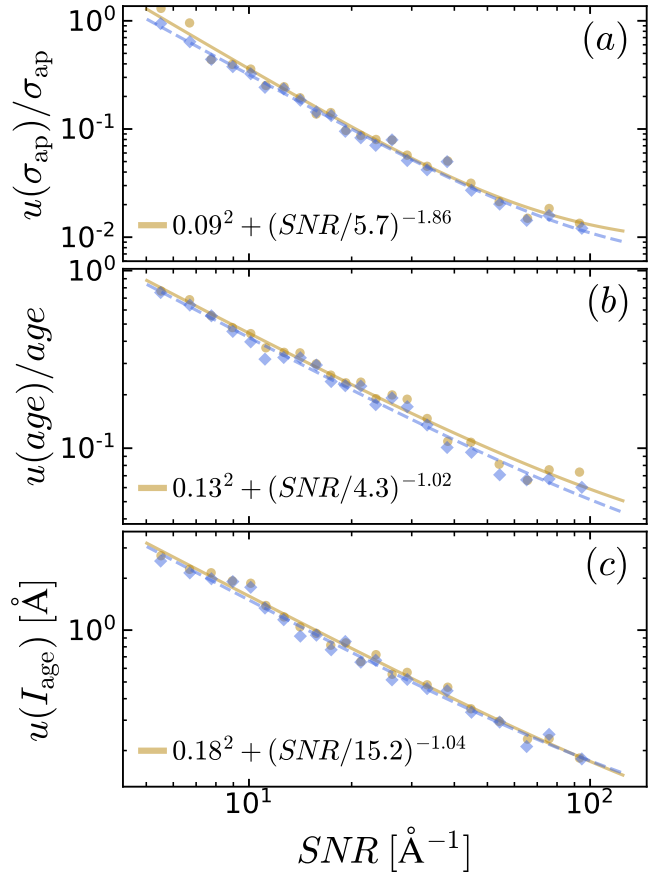


**Figure 4.** Measurement uncertainties from repeat observations, as a function of empirical SNR, for  $\sigma_{\text{ap}}$  (panel a), *age* (panel b) and the empirical index  $I_{\text{age}}$  (panel c). The golden circles are measurement uncertainties derived from repeat observations; these are obtained by binning the difference between repeats in SNR, removing pairs where the two SNRs differ by more than 50 per cent, then taking the standard deviation of the difference in each bin (divided by  $\sqrt{2}$ ). The solid golden lines are best-fit relations, which we use to estimate the measurement uncertainty on our data. Blue diamonds/dashed lines are the same, but rejecting pairs where the SNRs differ by more than 10 per cent. These uncertainties do not account for systematic errors (see e.g. Fig. 5), but systematics are not relevant to our analysis.

all parameters, taken singly, are statistically consistent with Eq. (4). From here on, we use the more conservative estimate of the uncertainties on *age* as inferred from Eq. (4).

In Fig. 5a we compare our default ages to the measurements from Vaughan et al. (2022), also obtained using PPXF and the MILES SSP library. Grey dots are galaxies with  $\text{SNR} > 15 \text{ \AA}^{-1}$  and blue diamonds are galaxies from the FP sample (see § 2.8). Note that  $15 \text{ \AA}^{-1}$  is the 5<sup>th</sup> percentile of the SNR distribution of the FP sample, but the grey circles include both star-forming and quiescent galaxies. We further validate our results by comparing our default *age* measurements to the values obtained by replacing the MILES SSP library with the synthetic C3K library (Conroy et al. 2019) with MIST isochrones (Choi et al. 2016). The advantage of this synthetic library is that it has uniform coverage in age-metallicity space, whereas MILES has lim-

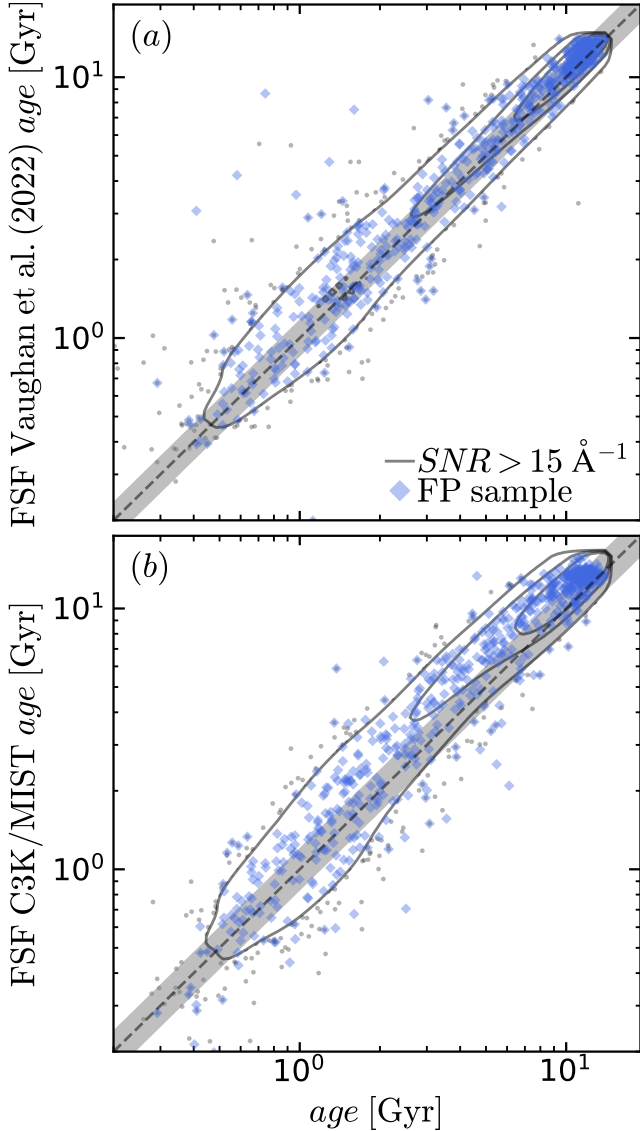


**Figure 5.** Comparison of our default age measurements (from full spectral fitting, using the MILES SSP library, labelled *age*) to two alternative age measurements: the measurements obtained with the methodology fo Vaughan et al. (2022, panel a), and the measurements obtained using a different SSP library (panel b). The contours enclose the 30<sup>th</sup>, 50<sup>th</sup> and 90<sup>th</sup> percentiles of the distribution of all galaxies with  $SNR > 15 \text{ \AA}^{-1}$  (galaxies outside the 90<sup>th</sup>-percentile contour are represented by individual grey dots); the blue diamonds are the 703 FP galaxies from the mock with  $t_{\text{exp}} = 2$  hours. The strong systematics between the different age measurements underscore the importance of assumptions in measuring age, but we checked that our results do not depend on these assumptions.

ited coverage over the grid we use<sup>2</sup>. The C3K/MIST library has an age-metallicity grid consisting of 107 age bins with  $0.1 \text{ Myr} < \text{SSP age} < 20 \text{ Gyr}$  (uniformly spaced in log-age by 0.05 dex) and 12 metallicity bins with  $-2.5 < [Z/H] < 0.5$  (uniformly spaced by 0.5 dex). For our test, we removed all

SSP spectra with SSP age  $< 0.03 \text{ Gyr}$ , to match the age range of MILES. Despite this, differences between the grid of the two SSP libraries still persist, both in the metallicity grid and in the spacing of the 57 age bins. In Fig. 5b we compare our default age measurements to the values obtained using the (trimmed) C3K/MIST library (labelled ‘FSF C3K/MIST *age*’).

We have checked that replacing *age* with the measurements from Vaughan et al. (2022) or FSF C3K/MIST *age* in our analysis does not alter our general conclusions. We also tested our results by using the Lick-index based SSP-equivalent ages (Scott et al. 2017); even though these measurements are very different from their FSF equivalents (see e.g. McDermid et al. 2015), our conclusions are not affected.

In addition to *age*, we also retrieve the *r*-band stellar mass-to-light ratio,  $\Upsilon_*$ . This gives us two stellar-mass measurements, the default  $M_*$  calibrated from multi-band photometry and *i*-band absolute magnitude (Taylor et al. 2011), and a new  $M_*$  from *g*- and *r*-band spectroscopy and *r*-band absolute magnitude. The two measurements are compared in Fig. 6a, showing good agreement. The Spearman correlation coefficient between the two measurements of mass-to-light ratio is  $\rho = 0.5$ , with the probability  $P$  of no correlation being  $P < 10^{-10}$ .

We use virial mass from Cappellari et al. (2013a) as a benchmark, and find that photometric stellar masses give the same observed scatter as spectroscopic stellar masses (panels b and c). This is surprising, because spectroscopy gives access to much more information than photometry alone. This unexpected outcome could be due to photometric  $M_*$  using *i*-band photometry, which is redder than the *r*-band spectroscopy available in SAMI. A similar result was found by Hyde & Bernardi (2009) using SDSS data. Overall, we find that the stellar-mass plane (Hyde & Bernardi 2009) does not give a more precise scaling relation, even when based on photometric  $M_*$  (Appendix A).

## 2.6 A new empirical index

Our declared aim is to realise the gain in distance precision expected from adding stellar-population age to the FP. However, even if this attempt was successful, it retains a critical flaw because of how we measure the age of a galaxy’s stellar population. A comparison with  $\sigma_{\text{ap}}$  will illustrate the problem. To measure  $\sigma_{\text{ap}}$ , we use empirical stellar spectra and assume a Gaussian LOSVD. This might present problems if the library of stellar spectra (derived from the Milky Way) cannot reproduce the spectra of external galaxies, or if the LOSVD is not Gaussian. In practice, however, Milky Way based stellar templates reproduce very accurately most of the visible spectrum for all but the most massive galaxies (e.g. van de Sande et al. 2017, their fig. 25). Moreover, within at least  $1 R_e$ , LOSVD deviations from a Gaussian are small (e.g. D’Eugenio et al., in prep.). Past experience shows that comparing between different methods gives consistency to within a modest fixed scale error (e.g. Said et al. 2020). In contrast, stellar-population age measurements are either based on empirical stellar-population spectra (derived from Milky Way stars), or on theoretical spectra (which are difficult to calibrate in the age and chemical-abundance ranges where there are few or no Milky Way stars). This is often compounded by assumptions about the initial mass function

<sup>2</sup> Please refer to the MILES webpage

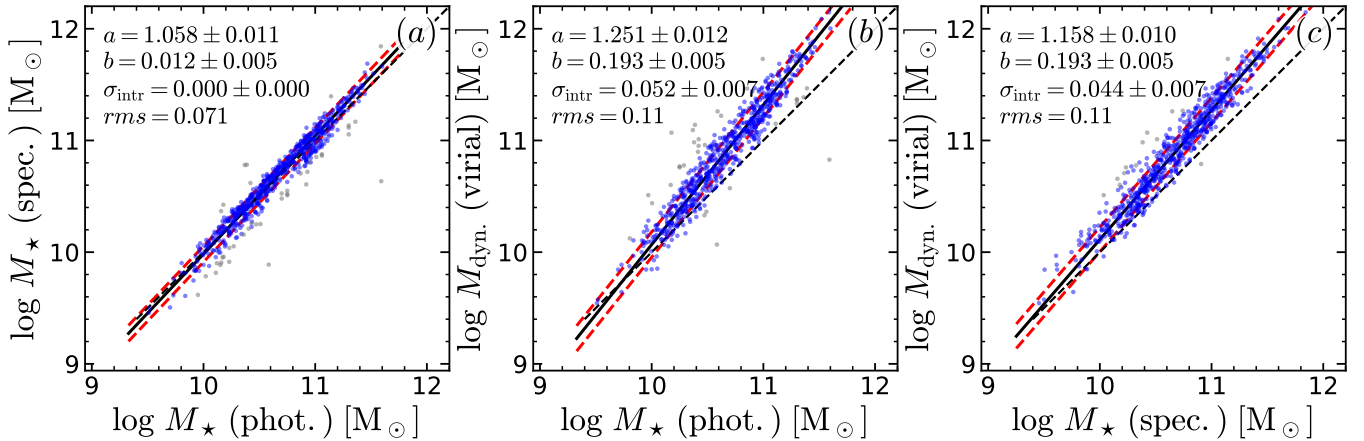


**Figure 6.** Comparison between photometric and spectroscopic  $M_\star$  (panel a, and their scaling with virial mass (panels b and c), which we use as a benchmark. Surprisingly, panels b and c have the same  $rms$ , which implies that  $M_\star(\text{phot.})$  is as precise as  $M_\star(\text{spec.})$ . This could be due to  $M_\star(\text{phot.})$  using information at longer wavelengths (*i*-band) which is not covered by SAMI spectroscopy.

and the star-formation history, as well as by the degeneracy between flux calibration uncertainties and the effects of age and dust. Full spectral fitting methods attempt to reproduce the whole optical spectrum, while methods based on spectral indices ‘condense’ the spectral information around specific spectral regions. Finally, some authors combine optical spectroscopy with broad-band photometry at bluer and redder wavelengths. In this broad and entangled landscape, age measurements are dominated by (non-linear) systematics, a polite way to state that often the measurements are driven by the method as much as the data. Fig. 5 shows an example of the magnitude of systematic age differences.

It is highly undesirable for a distance estimator to be dominated by systematics, because it hinders comparison between different works. For this reason, we define a new empirical index  $I_{\text{age}}$  to replace age in the FP. This index is the sum of five Lick indices

$$I_{\text{age}} \equiv \text{H}\delta_{\text{F}} + \text{H}\beta + \text{Fe}5015 - \text{Mgb} - \text{Fe}5406 \quad (5)$$

This index was derived empirically, by studying the sign and magnitude of the correlations between the FP residuals and the set of classic Lick indices. We did not attempt a more systematic search, such as ‘sequential feature selection’ (Ferri et al. 1994; e.g., Davis et al. 2022). Our current goal is to demonstrate a purely empirical measurement that could aid reducing the scatter of the FP, which we will demonstrate in Section 3. A more systematic search is left for future work. Note that we measure the indices at the native resolution of the SDSS data (including kinematic line broadening), without matching the spectral resolution of the original Lick definition. Thus our (pseudo) Lick indices contain both stellar population and stellar kinematics information. The measurement uncertainties on  $I_{\text{age}}$  are derived from repeat observations, similarly to  $\text{age}$  and  $\sigma_{\text{ap}}$ , obtaining

$$u(I_{\text{age}}) [\text{\AA}] = (0.18 \pm 0.11)^2 + \left( \frac{\text{SNR} [\text{\AA}^{-1}]}{15.2 \pm 0.6} \right)^{-(1.04 \pm 0.05)} \quad (6)$$

(solid golden line in Fig. 4c). Similarly to  $\sigma_{\text{ap}}$  and  $\text{age}$ , using the stricter cut at 10 per cent, we would get the same

uncertainties:  $0.21 \pm 0.12$ ,  $14.0 \pm 0.6$  and  $-1.09 \pm 0.06$ . (blue diamonds and dashed blue line in Fig. 4c). From here on, the uncertainties on  $I_{\text{age}}$  are inferred from Eq. (6). A comparison between  $I_{\text{age}}$  and the  $\text{H}\beta$  and  $\text{age}$  is provided in Fig. 7 (panels a and b, respectively).

## 2.7 Photometric and ancillary measurements

Our mass and size measurements are the same as DE21. We use best-fit total magnitudes and circularised half-light radii from Multi-Gaussian Expansion models (Emsellem et al. 1994), optimised using the publicly available algorithm MG-EFIT (Cappellari 2002). For more information about these measurements we refer the reader to DE21. Here we highlight three key aspects. First, these measurements result in different FP coefficients compared to e.g. Sérsic photometry (DE21, their table 3); this means that a quantitative comparison between our results and the literature is unwarranted. Second, we do not apply a *k* correction; as found by DE21, applying a *k* correction does not reduce the FP scatter, nor alters the correlation between the FP residuals and galaxy observables. Nevertheless, we remark that applying a *k* correction does not change our conclusions (we tested both the KCORRECT software of Blanton & Roweis 2007 and the polynomial approximation of Chilingarian et al. 2010, which gave median *k* correction values of 0.048 and 0.051 mag, respectively). Third, and perhaps most important point, we replace the average measurement uncertainties from DE21 with the average measurement uncertainties from H22; this does not change the observed FP scatter, but affects the relative contribution of measurement uncertainties and intrinsic scatter.

We use four ancillary measurements. Redshift  $z$  and stellar mass  $M_\star$  are taken from the SAMI DR3 catalogue (Croom et al. 2021;  $M_\star$  is obtained from *i*-band absolute magnitude  $M_i$  and  $g-i$  colour, following Taylor et al. 2011 and Bryant et al. 2015). The surface mass density  $\Sigma_\star$  is calculated as  $M_\star / (2\pi R_e^2)$ . Environment is measured using  $\Sigma_5$ , the surface density of galaxies inside the circle enclosing the five nearest neighbours (subject to  $M_r < -18.5$  mag within

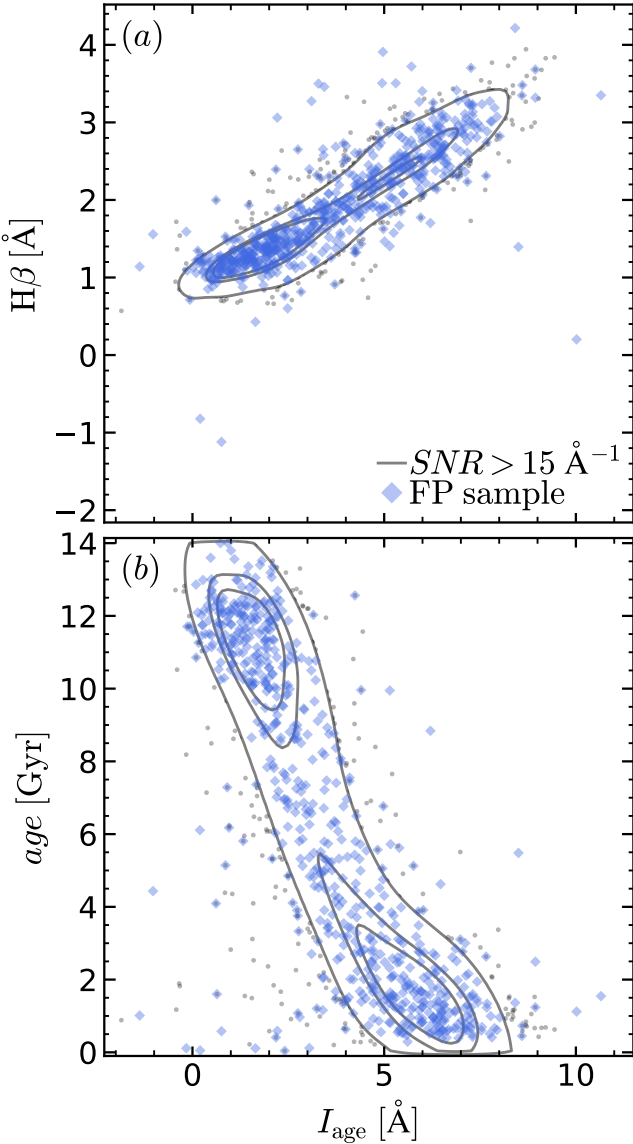


**Figure 7.** Comparing the index  $I_{\text{age}}$  to the  $H\beta$  Lick index (panel a) and to  $\text{age}$  (panel b; all symbols are the same as in Fig. 5).  $I_{\text{age}}$  is tightly correlated to  $H\beta$  and  $\text{age}$ ; the correlation with  $\text{age}$  means that, just like  $\text{age}$ ,  $I_{\text{age}}$  can be used to predict the FP residuals (see § 3.1, cf. Fig. 8b and c).

a range of velocity  $\Delta v < 500 \text{ km s}^{-1}$ , Brough et al. 2017). Note that, in § 5, we use SDSS data and a different environment measurement, group richness  $N_{\text{group}}$ . Finally, we measure  $\text{EW}(H\alpha)$ , the equivalent width of  $H\alpha$ , using PPXF to simultaneously model the continuum and emission-line spectra of the SAMI galaxies.

## 2.8 Sample selection

Our sample is selected as similarly as possible to that of Said et al. (2020) and H22. We require  $r$ -band apparent magnitude  $10 \leq m_r \leq 17$ , redshift  $0.0033 \leq z \leq 0.1$  (where for cluster galaxies we used the redshift of the cluster),  $r$ -band Sérsic index  $n \geq 1.2$  (this is equivalent to requiring a concentration  $R_{90}/R_e \geq 2.5$ ; note that not all SAMI galax-

ies have  $i$ -band Sérsic photometry, so we drop the similar requirement in this band), axis ratio  $b/a \geq 0.3$  in both  $r$ - and  $i$ -band<sup>3</sup>, colour  $g - i \geq 0.73 - 0.02(M_r + 20)$ , and aperture velocity dispersion  $\sigma_{\text{ap}} \geq 70 \text{ km s}^{-1}$ . We remove galaxies with strong  $H\alpha$  emission lines by requiring that the equivalent width is  $\text{EW}(H\alpha) > -1 \text{ \AA}$ . We further require that our galaxies are classified as early-type in their optical morphology, i.e.  $0 \leq \text{mtype} \leq 1$  (in the SAMI morphological classification, ellipticals have  $\text{mtype}=0$  and lenticulars have  $\text{mtype}=1$ ; see Cortese et al. 2016). These selection criteria result in 703 galaxies for each of the nine mock datasets with exposure times 0.125, 0.1875, ..., 2 hours; the mock sample with  $t_{\text{exp}} = 3$  hours contains only 665 galaxies, because 38 galaxies had SAMI observations with exposure time  $t_{\text{SAMI}} < 3$  hours.

## 2.9 Modelling the 3- and 4-dimensional planes

Systematics due to model choice dominate the uncertainties in the parameters of the FP (DE21). The three most popular models are an infinite plane with Gaussian scatter (either orthogonal or along the  $z$  axis, Cappellari et al. 2013a, Said et al. 2020, DE21; this model underlies  $\chi^2$  minimisation algorithms), an infinite plane with Laplacian scatter (usually orthogonal to the plane, de Graaff et al. 2020, 2021), and a 3-d Gaussian (with or without censoring, Saglia et al. 2001, Magoulas et al. 2012, Said et al. 2020, DE21). However, despite their differences, these models have in common that the residuals about the best-fit FP correlate most strongly with stellar population age (DE21). For this reason, in this work we use only a single model, based on the least trimmed squares, a robust  $\chi^2$  minimisation algorithm (LTS, Rousseeuw & Driessen 2006; we use the free implementation `LTS_PLANEFIT`, Cappellari et al. 2013a). The plane equation for the model underlying this ‘direct-fit’ method can be written as

$$r = a s + b i + d \quad (7)$$

where, from now on,  $s$ ,  $i$  and  $r$  are the logarithms of  $\sigma_{\text{ap}}$ ,  $\langle I \rangle_e$  and  $R_e$ . In the context of this work, this algorithm presents a key advantage over a multivariate Gaussian model: while extending a 3-d Gaussian to four dimensions increases the number of parameters from six to ten, extending Eq. (7) to four dimensions only requires one more parameter

$$r = a s + b i + c A + d \quad (8)$$

where  $A$  denotes the logarithm of  $\text{age}$ . We refer to this model as the 4-d hyperplane (dropping the adjective ‘fundamental’). We also consider the hyperplanes where  $A$  is replaced by  $I_{\text{age}}$ , or by  $v_* \equiv \log \Upsilon_*$ . We infer the uncertainties on the plane and hyperplane parameters from the measurement uncertainties on the data, which we assume to be Gaussian (we call these the ‘formal uncertainties’). These numbers, labelled  $u(a)$ ,  $u(b)$ , ... are reported as one standard deviation in the figures. For the mocks with 1 h exposure, we validated these uncertainties against bootstrapping the sample one hundred times. The two methods are in good agreement,

<sup>3</sup> A cut in galaxy shape is standard practice in FP cosmology, to avoid intrinsically flattened systems seen close to edge-on (Said et al. 2020, H22)

therefore we adopted everywhere the formal uncertainties, which are less computationally demanding.

### 3 THE HYPERPLANE OF EARLY-TYPE GALAXIES

To determine the impact of data quality on the 3-d FP and on the 4-d hyperplane, we find the best 3-d and 4-d fit for each of the ten sets of mock observations. For brevity, we show only example fits for the mock with 1 hour exposure time (§ 3.1). We then study the impact of spectral  $SNR$  on the FP and hyperplane coefficients (§ 3.2) and, most importantly, on the observed scatter (§ 3.3). We then study the presence and significance of correlations between the fit residuals and two key galaxy observables: stellar-population age and local environment density (§ 4; once again, in the interest of brevity, we only show the results for the mock with  $t_{\text{exp}} = 1$  hour). Finally, we study the effect of these two variables on the FP residuals, to assess whether they are independent (§ 4.1).

#### 3.1 Example best-fit planes

In Fig. 8 we show the FP and the three hyperplanes for the mock with  $t_{\text{exp}} = 1$  hour. Each panel shows measured vs predicted  $r$ , for the 3-d FP (panel a), for the 4-d  $age$  hyperplane (panel b), for the 4-d hyperplane using  $I_{\text{age}}$  (panel c), and for the 4-d hyperplane using mass-to-light ratio (panel d). Each of the 703 circles represents one SAMI galaxy, colour-coded by  $age$ . The best-fit coefficients from Eq.s (7–8) are reported in the top left corner of each panel (for the FP,  $c = 0$  by construction). We find  $\sigma_{\text{intr}} = 0.082 \pm 0.003$ ,  $0.064 \pm 0.003$ ,  $0.065 \pm 0.003$  and  $0.073 \pm 0.003$  respectively for the FP and for the age, index and mass-to-light ratio hyperplanes. This demonstrates that, for the adopted observing setup (1-hour integration on a 4-metre telescope), the 4-d hyperplane is able to utilise stellar-population information to reduce  $\sigma_{\text{intr}}$ . The magnitude of this improvement depends directly on our assessment of the random uncertainties, which are notoriously difficult to estimate accurately: overestimating the uncertainties would underestimate  $\sigma_{\text{intr}}$ . But this does not apply to the *observed* scatter (labelled  $rms$  in Fig. 8). We find  $rms = 0.089$ ,  $0.079$ ,  $0.078$  and  $0.083$ , so the 4-d hyperplanes are tighter than the FP — even accounting for the measurement uncertainties on  $A$ ,  $I_{\text{age}}$  and  $v_*$ . This reduced  $rms$  suggests that the hyperplanes could be used to derive more precise distances than the FP (§ 6.3).

The inset panels e–h show the fit residuals ( $\Delta r \equiv r - r_{\text{predicted}}$ ) as a function of  $age$ . For the FP there is a statistically significant correlation between  $\Delta r$  and  $age$  (panel e), which can also be appreciated as the clear trend in colour hue across the FP (panel a). This suggests that  $age$  contains information useful to reduce the FP scatter. In contrast, for the residuals of the hyperplanes, correlations with  $age$  are weaker (panel g and f) or not significant (panel f). This fact, coupled with the observation that the hyperplanes have smaller  $rms$  than the FP, confirms that the hyperplanes are tighter owing to the inclusion of stellar population information.

One may argue whether this stellar-population information is simply  $M_*$ , given the widely reported reduction

in scatter of the stellar-mass plane (Hyde & Bernardi 2009), obtained by replacing  $i$  with  $\log \Sigma_*$ . For our sample, the stellar-mass plane shows similar  $rms$  as the FP, but smaller  $\sigma_{\text{intr}}$ . A one-to-one comparison between the standard FP and the stellar-mass plane is reported in Appendix A.

#### 3.2 Best-fit parameters as a function of exposure time

In Fig. 9 we show the best-fit coefficients as a function of  $t_{\text{exp}}$  (and, equivalently, as a function of the median  $SNR$  over the whole sample,  $\langle SNR \rangle$ , reported on the bottom axis). As a benchmark, we report the equivalent exposure time of SDSS spectroscopy (vertical dashed line, see § 2.3). Each of panels a–d traces the homonym plane coefficient (cf. Eq.s (7–8); for the FP,  $c = 0$  and is not shown). The solid black line is for the FP, with the gray shaded regions encompassing the statistical uncertainties. We note that the FP coefficients depend on the quality of the spectra, particularly below the median  $SNR$  of SDSS. To find the value of  $a$  for  $t_{\text{SDSS}}$ , we interpolate linearly between  $t_{\text{exp}} = 0.25$  and  $0.375$  hours and get  $a = 1.142$ . This is 2.5 per cent larger than the limiting value at  $t_{\text{exp}} = 3$  hours (we find the same using the mean of all mocks with  $t_{\text{exp}} > 0.375$  hours). To our knowledge, this is the first time this effect is reported in the literature.<sup>4</sup> We find similar effects for  $b$  and  $d$ . The best-fit coefficients for the hyperplanes also show similar effects. We show the  $age$  hyperplane (dashed blue lines in Fig. 9), the  $I_{\text{age}}$  hyperplane (dash-dotted golden line) and the  $v_*$  hyperplane (dotted red lines). Compared to the FP coefficients, the hyperplanes coefficients converge at longer  $t_{\text{exp}}$ , in the range  $0.5 < t_{\text{exp}} < 1$  hour, depending on the coefficient and hyperplane flavour. The non-monotonic behaviour of  $b$ ,  $c$  and  $d$  below  $t_{\text{SDSS}}$  is due to the hyperplanes not converging for samples with  $\langle SNR \rangle < 25 \text{ \AA}^{-1}$ . Overall, we find that the FP parameters are very close to their ‘asymptotic’ values already for  $\langle SNR \rangle \approx 25 \text{ \AA}^{-1}$ , even though percent-level systematics seem to persist until a much higher  $\langle SNR \rangle \approx 40 \text{ \AA}^{-1}$ . It may be worth investigating whether a Bayesian approach can model out this bias, for instance, by introducing priors based on high-SNR observations.

#### 3.3 Observed scatter and residual correlations as a function of exposure time

In Fig. 10 we study the  $rms$  and residual correlations with  $age$  as a function of  $t_{\text{exp}}$ . From panel a, we see that the FP  $rms$  decreases only by  $\approx 10$  per cent across the whole range in  $t_{\text{exp}}$ ; in particular, the FP  $rms$  converges to its minimum  $rms$  already near  $t_{\text{SDSS}}$  (to within 2 per cent). The hyperplanes show different behaviours: they have larger/smaller  $rms$  than the FP for short/long  $t_{\text{exp}}$ . For the  $age$  hyperplane, equality is reached at  $t_{\text{exp}} \approx 0.375$  hours ( $\langle SNR \rangle \approx 28 \text{ \AA}^{-1}$

<sup>4</sup> This bias goes in the same direction as the reported difference in  $a$  between the optical and NIR FPs (M12), because the (optical) spectroscopy of the NIR FP has lower  $SNR$  than the (optical) spectroscopy of the optical FP, and the NIR-derived  $a$  is larger than the optical-derived  $a$ . Quantifying how much the effect we report contributes to the difference between the optical and NIR FPs is beyond the scope of this work.

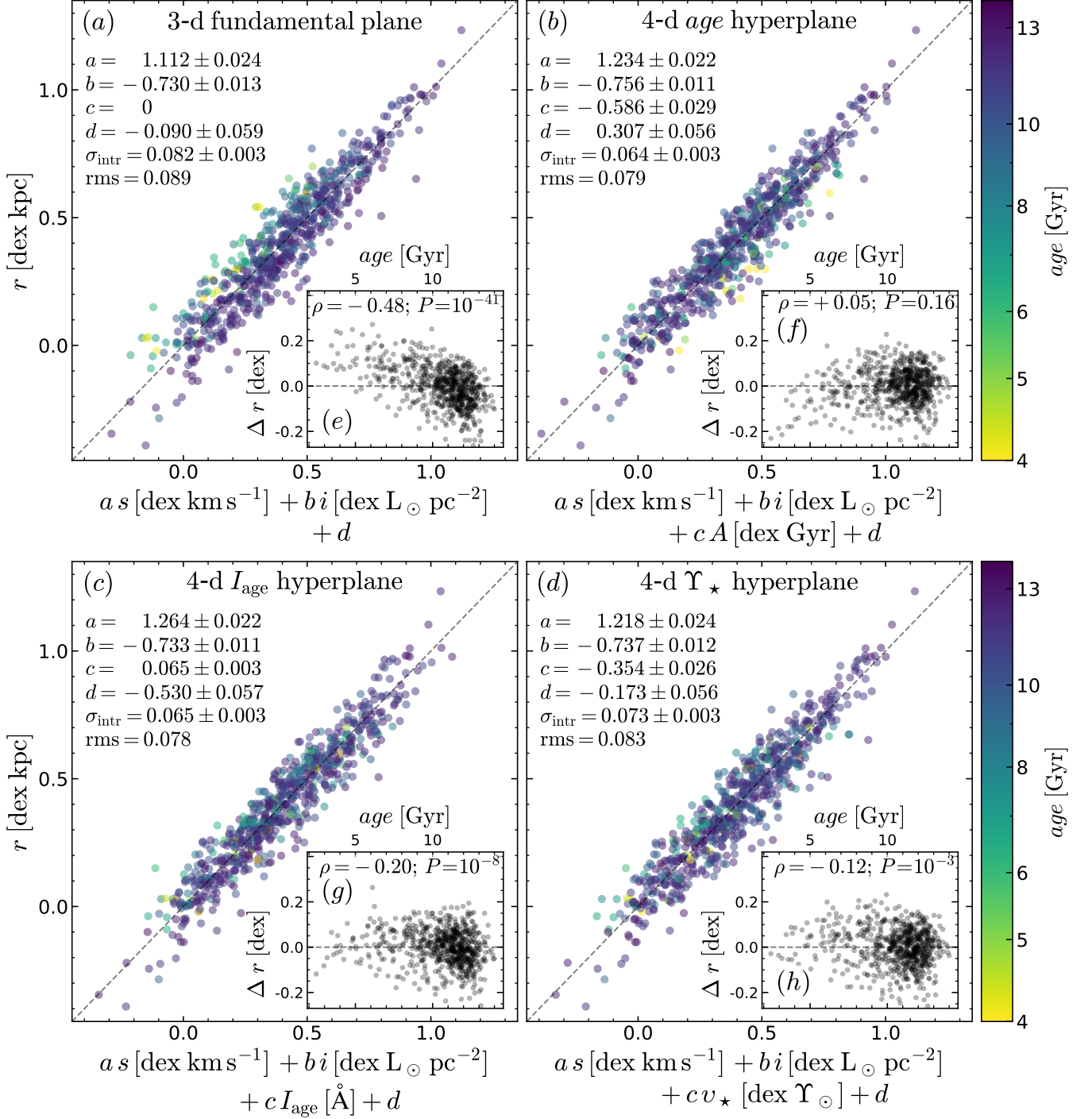


**Figure 8.** Predicted vs measured galaxy size, comparing the best-fit 3-d FP (panel a) to the 4-d hyperplane using either *age* (panel b),  $I_{\text{age}}$  (panel c), or  $\Upsilon_{\star}$  (panel d). Using fibres with 1.5-arcsec radius and an integration time of 1 hour with AAT/SAMI, the hyperplanes have both lower intrinsic scatter  $\sigma_{\text{intr}}$  and lower observed *rms*. Galaxies are colour-coded according to light-weighted stellar-population age. The inset panels e–h show the residuals  $\Delta r$  as a function of *age*: the correlation with the largest-magnitude coefficient and highest significance is for the FP. For  $I_{\text{age}}$  and  $\Upsilon_{\star}$ , the correlation is weaker and for the *age* hyperplane there is no correlation (see Fig. 10b).

<sup>-1</sup>). For the other two hyperplanes, our mocks show that equality is already reached near  $t_{\text{SDSS}}$  (vertical dashed line). For  $I_{\text{age}}$ , we tested this prediction using archival SDSS data and found it to be accurate (§ 5). Convergence to the

minimum *rms* occurs in the range 0.75–1.5 hours, i.e. for  $\langle \text{SNR} \rangle \approx 40\text{--}55 \text{ \AA}^{-1}$ .

In agreement with DE21, we find that the best predic-

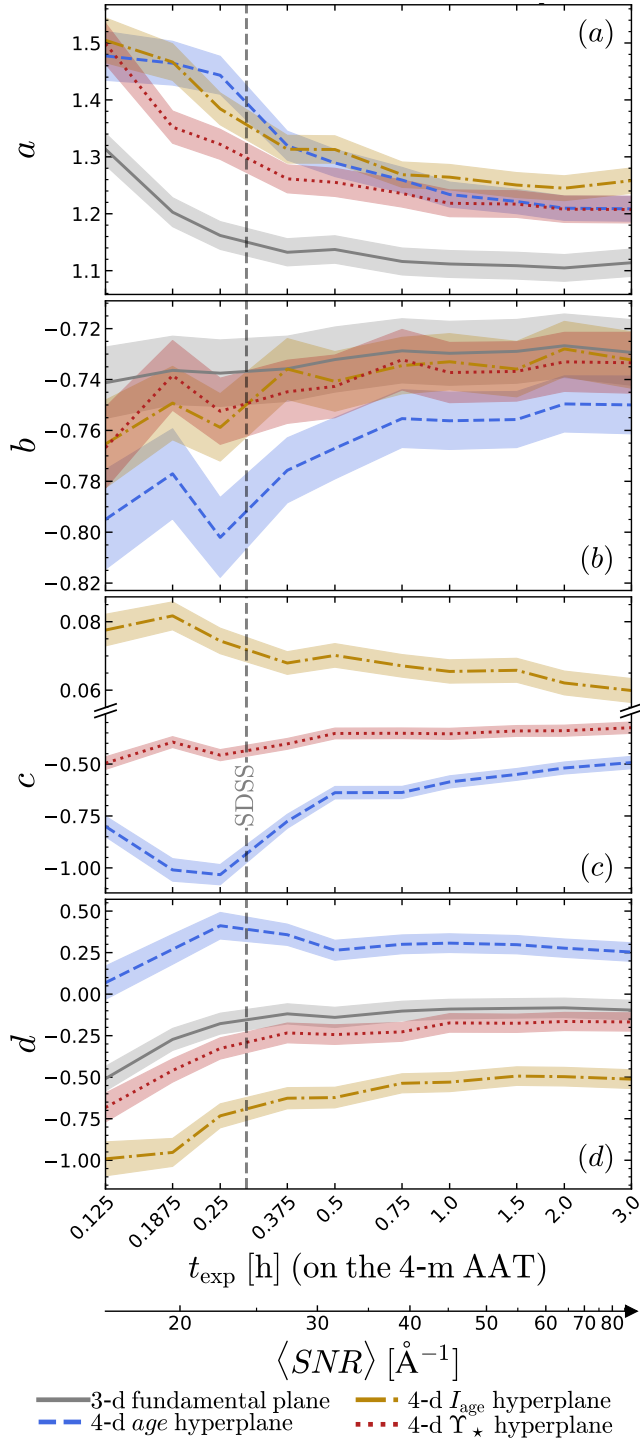


**Figure 9.** The best-fit FP and hyperplane coefficients as a function of the mock exposure time  $t_{\text{exp}}$  (and of the average sample  $\text{SNR}$ ,  $\langle \text{SNR} \rangle$ ). The dashed vertical line is  $t_{\text{SDSS}}$ . For  $t_{\text{exp}} < t_{\text{SDSS}}$ , the best-fit coefficients can be significantly different from their limiting values at high  $\text{SNR}$ . For the FP, convergence is already achieved at  $t_{\text{exp}} = t_{\text{SDSS}}$ ; for the hyperplanes, convergence requires  $t_{\text{exp}} \gtrsim 0.5$  hours. Note the broken y axis in panel c, to accommodate two different scales.

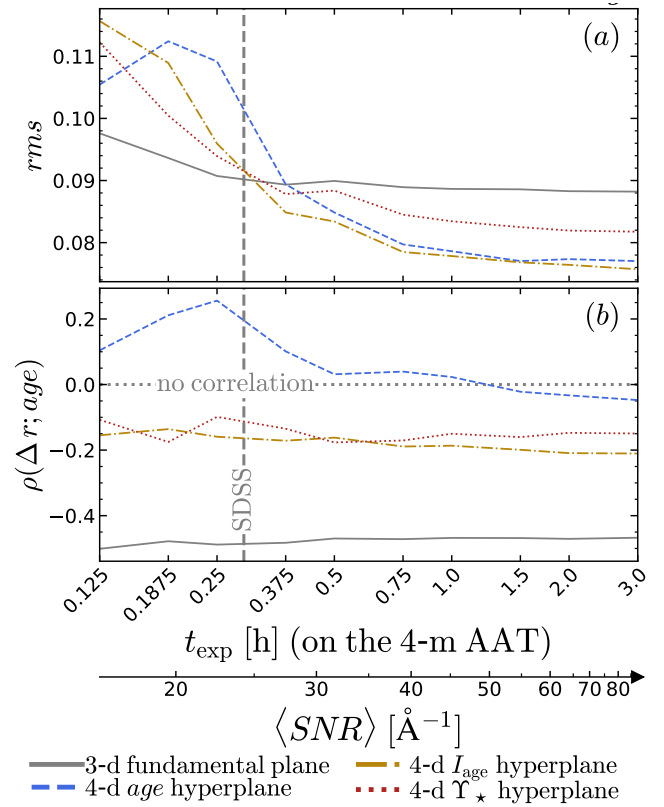


**Figure 10.**  $rms$  (panel a) and residuals–age correlation coefficient ( $\rho(\Delta r; \text{age})$ ; panel b) for the best-fit FP and hyperplanes, as a function of  $t_{\text{exp}}$  (and  $\langle \text{SNR} \rangle$ ). The lines are the same as in Fig. 9. For  $t_{\text{exp}} < t_{\text{SDSS}}$ , the FP (solid black line) has smaller  $rms$  than any of the hyperplanes (panel a). For  $t_{\text{exp}} \sim t_{\text{SDSS}}$ , the  $I_{\text{age}}$  and  $\Upsilon_{\star}$  hyperplanes have similar  $rms$  to the FP (dashed-dotted golden line and dotted red line). Finally, for  $t_{\text{exp}} > t_{\text{SDSS}}$ , all the hyperplanes (including the age hyperplane, dashed blue line) have smaller  $rms$  than the FP. Regardless of  $t_{\text{exp}}$ , the FP always displays a correlation between the residuals  $\Delta r$  and age (panel b). Adding a fourth observable to the FP reduces the magnitude of this correlation, even with short  $t_{\text{exp}}$  (low  $\langle \text{SNR} \rangle$ ). However, to also reduce the  $rms$ , this fourth observable must be sufficiently precisely determined that its random measurement uncertainties do not negatively offset the gain due to the additional information they provide.

<sup>5</sup> of the FP  $\Delta r$  is age. Indeed, for the FP, the anticorrelation has Spearman correlation coefficient  $\rho(\Delta r; \text{age}) = -0.5-0.45$  (panel b). For the age hyperplane, we find positive correlation below 0.5 hours, and no correlation above it, suggesting that age information has been used to reduce the  $rms$ . Interestingly, for the other two hyperplanes,  $\Delta r$  still anticorrelates with age (albeit with less than half the FP magnitude). For the  $\Upsilon_{\star}$  hyperplane, one can argue age information was not correctly encapsulated in the fit, which explains why its  $rms$  is larger than for the age hyperplane. However, for the  $I_{\text{age}}$  hyperplane, the  $rms$  is the same as the age hyperplane, yet  $\rho$  has larger magnitude. This means

<sup>5</sup> Here and afterwards, the ‘best predictor’ of  $\Delta r$  has the correlation coefficient with the largest magnitude and highest statistical significance, as in DE21.

that  $I_{\text{age}}$  taps in part information other than  $age$  to reduce the FP scatter.

To first order, the precision of the FP as a distance indicator can be gauged from its observed  $rms$ . Comparing this value between the three hyperplanes (Fig. a), we find that  $\Upsilon_*$  yields the largest  $rms$  of the three. The other two implementations, the  $age$  and  $I_{\text{age}}$  hyperplanes are comparable to one another and have substantially lower  $rms$ , but  $I_{\text{age}}$  has the critical advantage of being an empirical observable, measurable directly from the spectra without any additional assumptions (cf. § 2.6). For this reason, from now on, we focus on the  $I_{\text{age}}$  hyperplane.

#### 4 RESIDUAL CORRELATIONS WITH ENVIRONMENT

The existence of residual correlations between  $\Delta r$  and local environment (M12, H22) is worrying for cosmological applications, because FP-derived distances would place galaxies in under/overdense environments systematically closer/further than their true distance. In this section, we study the strength and significance of this residual correlation for the FP and for the  $I_{\text{age}}$  hyperplane. As a comparison, we use the  $\Delta r$ - $age$  anticorrelation, the best predictor of  $\Delta r$ . As a measure of local environment, we use  $\Sigma_5$  (§ 2.7).

In the left column of Fig. 11 we show the FP  $\Delta r$  as a function of  $age$  (panel a) and  $\Sigma_5$  (panel c). Each panel reports the value of  $\rho$  and its significance  $P$ . Both  $age$  and  $\Sigma_5$  correlate with  $\Delta r$ , but, in agreement with DE21, the correlation with  $age$  has larger magnitude and higher statistical significance.

In the right column of Fig. 11, we show  $\Delta r$  for the  $I_{\text{age}}$  hyperplane. For  $age$ ,  $\rho$  is now less than half the FP value (and its statistical significance is also lower, panel b); for  $\Sigma_5$ , the change is even more dramatic:  $\rho$  is only about one fourth the FP value, and its significance is marginal (2- $\sigma$ , panel d).

This result shows that the correlations of  $\Delta r$  with  $age$  and  $\Sigma_5$  are not independent. By correcting the FP for  $I_{\text{age}}$  (which encodes in part  $age$  information) the 4-d hyperplane also greatly reduces, or even eliminates, the problem of the environment bias of FP distances.

##### 4.1 Relation between age and local environment

Given the correlation between environment density and  $age$ , which is the physical driver between the  $\Delta r$ - $\Sigma_5$  and  $\Delta r$ - $age$  correlations? To address this question, we use the method of partial correlation coefficients (hereafter, PCC; see e.g. Bait et al. 2017; Bluck et al. 2019; Baker et al. 2022). In general, if two variables  $x$  and  $z$  are both independently correlated with a third variable  $y$ , then this will induce an apparent correlation between  $y$  and  $z$ . PCCs address this issue by quantifying the strength and significance of the correlation between  $y$  and  $z$  while controlling for  $x$ . Similarly to the standard Spearman rank correlation coefficient, a value of zero implies no correlation, and  $-/+1$  implies perfect anti/correlation. In the following, we denote with  $\rho(x, z|y)$  the partial correlation coefficient between  $x$  and  $z$  removing the effect of  $y$ .

In Fig. 12, we show the  $age$ - $\Sigma_5$  plane, colour-coded by

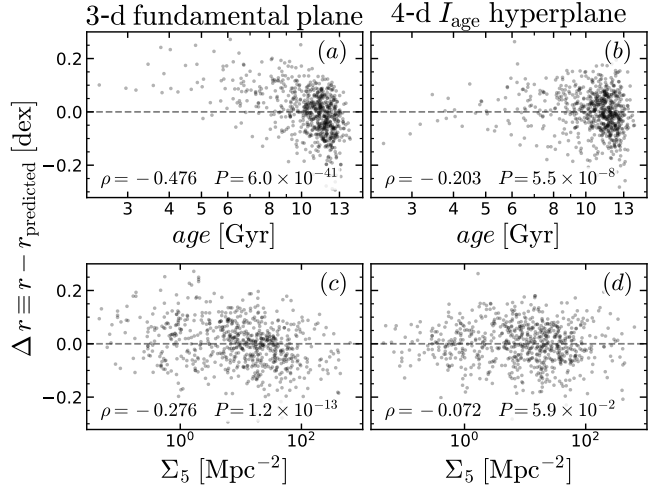


**Figure 11.** Residuals  $\Delta r$  of the 3-d FP (left column) and of the 4-d  $I_{\text{age}}$  hyperplane (right column) as a function of stellar population age (top row) and local environment density (bottom row). Each panel also reports the Spearman rank correlation coefficient  $\rho$  and the corresponding  $P$  value. For the FP,  $\Delta r$  correlates with both  $age$  and  $\Sigma_5$ . For the hyperplane,  $\Delta r$  has a much weaker (but still significant) correlation with  $age$ , while the correlation with  $\Sigma_5$  is weaker and only marginally significant. Note panels a and b are the same as panels e and g from Fig. 8, and are reproduced here for convenience.

the FP residuals  $\Delta r$  (here  $\Delta r$  has been smoothed using the robust locally-weighted regression algorithm of Cleveland & Devlin 1988 and Cappellari et al. 2013b, LOESS). Regions of uniform colour hue are tilted with respect to the axes, highlighting that  $age$  and  $\Sigma_5$  have independent roles. Controlling for  $\Sigma_5$ , we find  $\rho(\Delta r, age|\Sigma_5) = -0.44$ , with  $P = 9.9 \times 10^{-34}$ , whereas controlling for  $age$ , we find  $\rho(\Delta r, \Sigma_5|age) = -0.14$ , with  $P = 3.4 \times 10^{-4}$ . Thus  $\Delta r$  correlates independently with both  $age$  and  $\Sigma_5$ , but the correlation with  $age$  is both stronger (higher-magnitude correlation coefficient) and more significant. The relative importance of the two correlations can be visualised using the arrow representation of the ratio of PCCs (introduced by Bluck et al. 2020). We obtain an angle of  $(197 \pm 12)^\circ$  (black arrow in Fig. 12; the grey arrows represent the 1<sup>st</sup>-99<sup>th</sup> percentiles from bootstrapping the sample one thousand times). The arrow is almost parallel to the  $age$  axis, indicating that for the FP  $\Delta r$  is driven almost entirely by  $age$ , and the independent correlation with environment plays only a secondary role, if at all. Thus the  $\Delta r$ - $\Sigma_5$  anticorrelation is mostly due to the known correlation between the  $\Delta r$  and  $age$ , combined with the correlation between  $age$  and  $\Sigma_5$ . This explains why, in correcting for the  $age$  bias, the 4-d hyperplanes provide the environment bias correction for free (§ 4).

#### 5 APPLICATION TO THE SDSS SAMPLE

In the previous two sections we have made two key statements:

- The hyperplanes have lower  $rms$  than the FP (for sufficiently high  $SNR$ ; § 3.3, Figs 8 and 10);
- By removing the  $age$  bias from the FP, the hyperplanes

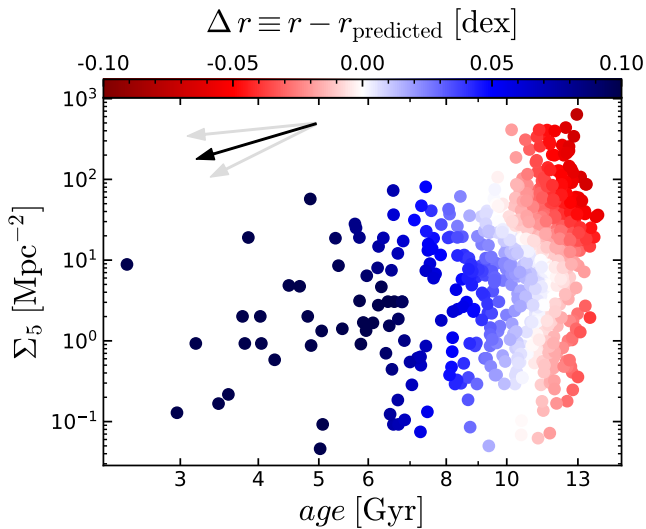


**Figure 12.** Distribution of the FP residuals  $\Delta r$  on the  $age$ – $\Sigma_5$  plane.  $\Delta r$  has been LOESS smoothed to highlight the trend. The arrow is a graphical representation of the partial correlation coefficients; it has an angle of  $(197 \pm 12)^\circ$ , with the uncertainties encompassing the 1<sup>st</sup> and 99<sup>th</sup> percentiles. An angle of  $180^\circ$  would correspond to perfect anti-correlation between  $\Delta r$  and  $age$ , and no independent correlation with  $\Sigma_5$ .  $\Delta r$  is strongly dominated by  $age$ , with only a weak independent anti-correlation with  $\Sigma_5$ .

also remove the environment bias (as measured by  $\Sigma_5$ ; § 4, Fig. 11)

Both these statements are based on data from SAMI, which we degraded to simulate the effect of lower- $SNR$ , single-fibre observations. In this section, we test these two hypotheses using independent data from SDSS. The sample consists of 34,059 galaxies from H22. This sample is originally drawn from the SDSS Data Release 14 (Abolfathi et al. 2018), with the criteria very similar to those summarised in § 2.8. To these measurements, we added our own Lick-index and  $age$  measurements, using the methods outlined in § 2.6. This results in a sample of 31,909 galaxies. There is a key difference between this sample and SAMI; for SAMI, we measure *local* environment (using  $\Sigma_5$ ), but for SDSS we measure *global* environment (using  $N_{\text{group}}$ , the number of galaxies in the group, Tempel et al. 2017).

In § 3.3, we have shown that the  $I_{\text{age}}$  hyperplane has the same  $rms$  of the FP, already for exposure time  $t_{\text{exp}} = 0.3$  hours on the 4-metre AAT Telescope. This is roughly equivalent to the depth of the SDSS data (0.75 hours on the 2.5-metre APO Telescope; dashed vertical line in Fig. 10a). The FP and the  $I_{\text{age}}$  hyperplane are shown in Fig. 13; as predicted from the  $rms$ – $t_{\text{exp}}$  relation for  $t_{\text{exp}} = t_{\text{SDSS}}$  (Fig. 10b), these two scaling relations have comparable  $rms$ : 0.085 dex for the FP (panel a) and 0.087 dex for the hyperplane (panel b); the median distance uncertainties is 0.085 dex for both distance indicators.

At the large-size (high-mass) end of the FP, adding  $I_{\text{age}}$  information *increases* the scatter. This is what we expect if the scatter is driven by stellar mass-to-light ratio, which is highly degenerate at the high-mass end and therefore requires high- $SNR$  measurements to disentangle. Conversely, at the small-size (low-mass) end of the FP, adding  $I_{\text{age}}$  information reduces the  $rms$ . Overall, at the  $SNR$  level of the

SDSS data, the two effects compensate and the hyperplane has comparable  $rms$  to the FP. We further notice that in the FP, the oldest galaxies (yellow hues in Fig. 13) lie preferentially below the plane, forming a tighter sequence with steeper slope; conversely, the youngest galaxies (blue hues) lie preferentially above the plane. So these two extremes of the  $age$  distribution occupy different regions of the parameter space, such that selecting on observables that correlate with  $age$  (e.g.,  $\sigma_{\text{ap}}$ ) may alter the best-fit FP slope (D’Onofrio et al. 2008).

Crucially, when we study the fit residuals, we find a statistically significant trend with environment for *both* the FP and the  $I_{\text{age}}$  hyperplane, unlike what we found based on SAMI data (Fig. 13d and e). The magnitude of the Spearman’s rank correlation coefficient is largest for the FP residuals, so the  $I_{\text{age}}$  hyperplane reduces the environment bias. However, the remaining bias is still large ( $\rho = -0.118$ ) and highly significant.

## 5.1 The SDSS $age$ hyperplane

Fig 13c shows the  $age$  hyperplane for SDSS, compared again to the FP. Here the  $rms$  and distance uncertainties are larger than for the FP — again in agreement with the SAMI predictions, given the depth of the SDSS spectra (Fig. 10a). However, for the  $age$  hyperplane, the correlation between the residuals and environment is only marginally significant ( $\rho = -0.01$ ,  $P = 0.04$ ); comparing these values to the corresponding results for the FP ( $\rho = -0.137$ ,  $P < 10^{-10}$ ), we conclude that the  $age$  hyperplane is effectively free from the environment bias affecting the FP.

Using partial correlation coefficients to study the interplay between the FP  $\Delta r$ ,  $age$  and  $N_{\text{group}}$ , we find that  $\rho(\Delta r, age | N_{\text{group}}) = -0.45$ , whereas controlling for  $age$ , we find  $\rho(\Delta r, N_{\text{group}} | age) = -0.09$ . While both results are statistically significant, this shows that the correlation of the FP residuals  $\Delta r$  with  $N_{\text{group}}$  is driven primarily by the combination of the  $\Delta r$ – $age$  correlation with the  $age$ – $N_{\text{group}}$  correlation. Note that — in agreement with H22 — we find that absolute magnitude  $M_r$  does not explain the  $\Delta r$ – $N_{\text{group}}$  correlation; we find  $\rho(\Delta r, N_{\text{group}} | M_r) = -0.15$ , very similar to the regular Spearman’s rank correlation coefficient between  $\Delta r$  and  $N_{\text{group}}$  ( $\rho = -0.137$ , Fig. 13d).

## 6 DISCUSSION

### 6.1 Physical meaning: $age$ and mass-to-light ratio

For virialised galaxies, the FP intrinsic scatter  $\sigma_{\text{intr}}$  must arise from the conversion between the dynamical quantities in the virial theorem<sup>6</sup> and the observables constituting the FP. Indeed, dynamical models based on IFS data form a mass (or virial) plane consistent with  $\sigma_{\text{intr}} = 0$  (Cappellari et al. 2013a). For these models, the key to eliminating  $\sigma_{\text{intr}}$  is in the *total* mass-to-light ratio, including dark matter ( $\approx 20$  per cent) and IMF variations (Cappellari et al. 2013b). However, accurate dynamical models require spatially resolved spectroscopy, which is still too expensive for large cosmological surveys.

<sup>6</sup> Including the structural coefficient

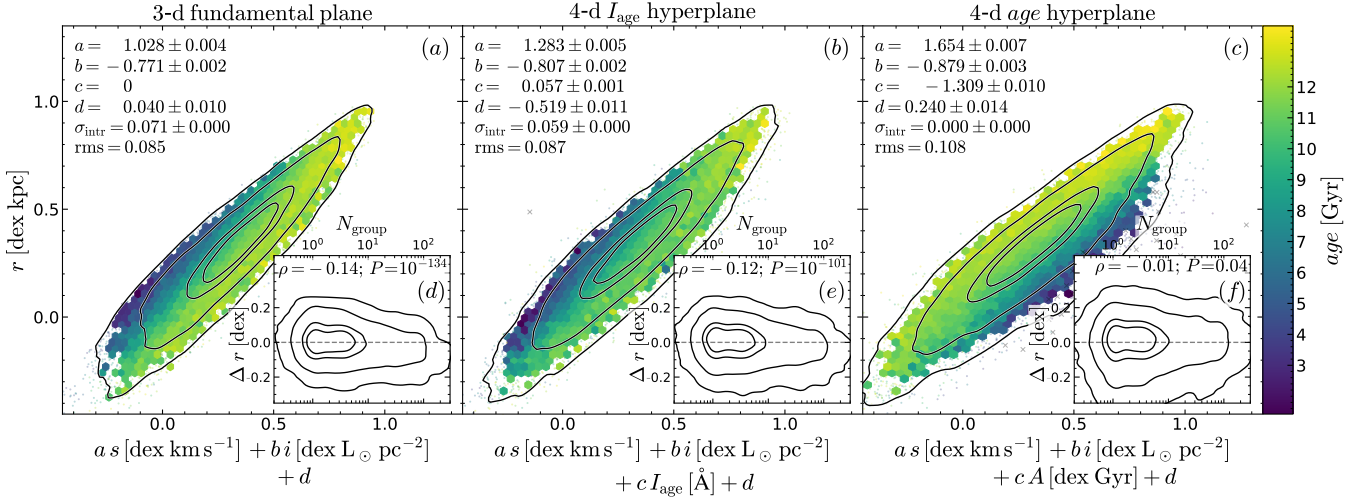


**Figure 13.** Predicted vs measured galaxy size using data from SDSS. The 3-d FP (panel **a**) has the same  $rms$  as the 4-d  $I_{age}$  hyperplane (panel **b**). The median uncertainty of the two samples is comparable, in agreement with the results of our mock observations (see § 6.3). In contrast, the  $age$  hyperplane has larger  $rms$ , also in agreement with SAMI-based predictions. Bins contain a minimum of five galaxies and are colour coded by their mean  $age$ ; individual galaxies are represented by dots. The inset panels show the correlation between the fit residuals and global environment  $N_{group}$ . The FP and  $I_{age}$  hyperplanes display the correlation reported by H22, whereas for the  $age$  hyperplane there is no residual correlation.

Among the observables we can obtain from photometry or single-fibre spectroscopy, a number of works argued that stellar-population properties — and  $age$  in particular — are good predictors of the FP residuals  $\Delta r$  (Gregg 1992; Prugniel & Simien 1996; Forbes et al. 1998; Graves et al. 2009; Falcón-Barroso et al. 2011; Springob et al. 2012; Yoon & Park 2020). In particular, DE21 performed a comparative analysis of various structural and stellar-population observables, finding that  $age$  is the best predictor of  $\Delta r$ . Indeed, this prediction is consistent with the fact that — for sufficiently high  $\langle SNR \rangle$  — the  $age$  hyperplane has lower observed  $rms$  than the FP (Figs 8a–b and 10a) and the  $\Delta r$ – $age$  correlation disappears (Fig. 10b).

In principle, replacing  $age$  with  $\Upsilon_*$  brings the hyperplane closer to the virial plane (DE21, their eq. 2) so it should further reduce  $\sigma_{intr}$ . But in practice  $\Upsilon_*$  gives larger observed  $rms$  than  $age$ , pointing to significantly larger measurement uncertainties — particularly so, given that the best-fit coefficient of  $\Upsilon_*$  is 30 per cent smaller (in magnitude) than the coefficient of  $age$  (Fig. 9c). Indeed, we find a median uncertainty on  $\Upsilon_*$  of 0.05 dex for the 1 h mock (and 0.04 dex for the 2 h mock; the corresponding values for  $age$  are just 10 per cent smaller). For  $\Upsilon_*$ , these estimates are in agreement with the lowest estimates from Gallazzi & Bell (2009) and might indeed be too optimistic. If the larger  $rms$  of the  $\Upsilon_*$  hyperplane was due entirely to underestimated measurement uncertainties on  $\Upsilon_*$ , then their median value must be *at least* 0.08 dex (more in line with the upper estimate from Gallazzi & Bell 2009). Intriguingly, these larger uncertainties are not captured by our method (which compares repeat observations, using the procedure described in § 2.4 for  $\sigma_{ap}$ ). The  $\Upsilon_*$  hyperplane could represent an independent testing bench to compare the precision of different spectro-photometric fitting algorithms and modelling assumptions.

Alternatively,  $age$  might contain additional information

that is not captured by  $\Upsilon_*$ . For example, in addition to  $\Upsilon$  variations at fixed IMF,  $age$  might correlate with the true stellar  $\Upsilon$ , i.e., including systematic IMF variations; this could be via the empirical correlations between  $age$  and  $\sigma$  (e.g., Gallazzi et al. 2005; McDermaid et al. 2015; Barone et al. 2018), and between  $\sigma$  and IMF parameters (Cappellari et al. 2013b). Alternatively,  $age$  may contain some structural and/or dynamical information, as evidenced by the fact that  $age$  is the best predictor of the spin parameter  $\lambda_R$  (Croom et al. 2024), which captures the degree of rotation support in galaxies (Emsellem et al. 2011); after all, early-type galaxies with different values of  $\lambda_R$  show different behaviours on the FP (Bernardi et al. 2020).

## 6.2 Physical meaning: spectral index

Moving to the  $I_{age}$  hyperplane, we find it to have the same or even smaller  $rms$  than both the FP and even the  $age$  hyperplane (Fig. 10a). However, unlike for the  $age$  hyperplane,  $\Delta r$  still anticorrelates with  $age$  (panel **b**). This means that to achieve the same reduction in  $rms$  as the  $age$  hyperplane,  $I_{age}$  draws in part from information that is not contained in  $age$ . This raises two pressing questions. First, what is this information? And second, can we combine it with  $age$  to reduce the  $rms$  even further?

After  $age$ , the second best predictor of the FP  $\Delta r$  is  $[\alpha/Fe]$ , the abundance of  $\alpha$  elements relative to iron (DE21). This information could be ostensibly present in  $I_{age}$  via the Mgb index. The feasibility of leveraging  $[\alpha/Fe]$  to reduce the FP  $rms$  has already been proven (Gargiulo et al. 2009). In DE21 we argued that the  $\Delta r$ – $[\alpha/Fe]$  anticorrelation was also present at fixed  $age$ , which here we confirm and quantify using PCCs: regardless of how we measure  $[\alpha/Fe]$ , the  $\Delta r$ – $[\alpha/Fe]$  anticorrelation exists independently from the  $\Delta r$ – $age$  anticorrelation, with a correlation coefficient that is roughly one third the coefficient of  $\Delta r$ – $age$  (Appendix B). If

$[\alpha/\text{Fe}]$  was indeed the information  $I_{\text{age}}$  uses, the partial independence of the  $\Delta r$ - $[\alpha/\text{Fe}]$  and  $\Delta r$ - $\text{age}$  relations makes it worthwhile attempting to combine  $\text{age}$  and  $[\alpha/\text{Fe}]$  to further reduce the  $\text{rms}$  compared to the  $\text{age}$  and  $I_{\text{age}}$  hyperplanes. Indeed, studying the residuals of the  $\text{age}$  hyperplane, we find an anticorrelation with  $[\alpha/\text{Fe}]$ , with  $\rho = -0.20$  and  $P = 1.8 \times 10^{-7}$ . These values place  $[\alpha/\text{Fe}]$  among the best predictors of the residuals of the  $\text{age}$  hyperplane — and in first place if we exclude observables that appear (directly or indirectly) in the hyperplane (e.g., luminosity, surface brightness, size).

Physically,  $[\alpha/\text{Fe}]$  is not a strong driver of  $\Upsilon_*$ , so it is unclear how it can predict  $\Delta r$  even after controlling for  $\text{age}$ . Repeating the arguments of DE21,  $[\alpha/\text{Fe}]$  may be capturing age information that is too degenerate for  $\text{age}$  itself, or, alternatively, might correlate with some of the other observables that relate the FP to the virial plane: dark-matter fraction and IMF shape. We note here the latter would be more natural. This is because, compared to low-dispersion galaxies, high-dispersion galaxies have both higher  $[\alpha/\text{Fe}]$  (Trager et al. 2000; Thomas et al. 2010; McDerimid et al. 2015; Scott et al. 2017; Watson et al. 2022a,b — but see Liu 2020 for a different view) and more bottom-heavy IMFs (Cappellari et al. 2013b). The latter increases the mass-to-light ratio above the average value, thus causing the  $\Delta r$ - $[\alpha/\text{Fe}]$  anticorrelation. In contrast, the sign of this anticorrelation would require that high- $[\alpha/\text{Fe}]$  galaxies have the largest central dark-matter fractions, which runs contrary to the results of dynamical models (Cappellari et al. 2013a). Investigating the joint use of  $[\alpha/\text{Fe}]$  and  $\text{age}$  (or  $I_{\text{age}}$ ) is beyond the scope of this article.

Clearly, other explanations are also possible as to what information  $I_{\text{age}}$  contains but  $\text{age}$  does not.

### 6.3 Breakdown of the distance uncertainties

We have seen that, for an exposure time of 1 hour, the 4-d hyperplanes have less intrinsic and observed scatter than the 3-d FP. The critical question, however, is whether this translates into increased precision on the derived distances. The risk, as shown by M12 for the  $\text{age}$  hyperplane, is that large measurement uncertainties on  $\text{age}$  may frustrate the improvement in scatter between the 3-d and 4-d relation. Moreover, in most real applications, higher  $\text{SNR}$  comes at the expense of smaller sample size, so it is critical to find the tradeoff between these two aspects of a survey. To establish whether, and under what conditions, the 4-d hyperplane yields more precise distances, we estimate the uncertainty on hyperplane-derived distances by using the error propagation formula

$$u_{4d}^2(\text{dist}) \equiv \sigma_{\text{intr}}^2 + u^2(d) + u^2(r) + (u^2(a)s^2 + a^2u^2(s)) + (u^2(b)i^2 + b^2u^2(i)) + (u^2(c)X^2 + c^2u^2(X)) \quad (9)$$

where  $u(x)$  is the uncertainty on any given quantity  $x$ ,  $X$  is either  $A$ ,  $I_{\text{age}}$  or  $v_*$ , depending on the hyperplane considered, and the expression for  $u_{3d}(\text{dist})$  is readily obtained by setting  $c = 0$  and  $u(c) = 0$ . The measurement uncertainties on the hyperplane observables  $r$ ,  $s$  and  $i$  have been estimated in § 2, whereas the uncertainties on the hyperplane parameters are obtained directly from the fit (we checked that these values are consistent with the values obtained by

bootstrapping the sample). The value of the distance uncertainty varies from galaxy to galaxy, so to simplify our analysis we consider only the median uncertainty value over the whole sample. In Fig. 14 we show the total uncertainty (dashed black line) and each of the individual addends; note that we show the *squares of the uncertainties*, to preserve the linearity of Eq. (9); the uncertainties themselves are shown in Fig. 15. We further note that the parameter uncertainties  $u(a)$ ,  $u(b)$ ,  $u(c)$  and  $u(d)$  decrease approximately as the square root of the sample size. For this reason, for our sample of only 703 galaxies, these uncertainties have a disproportionate contribution compared to what they would have for a typical cosmology application of the FP, which might utilise several thousand galaxies (e.g. Said et al. 2020). To simulate their relative importance on a cosmological survey of 5000 galaxies, we divide each of these values by  $\sqrt{5000/703}$ ; further, we simulate a survey of finite total integration time. This implies that the sample size decreases with increasing exposure time. To include this effect, we further multiply the parameter uncertainties  $u(a)$ - $u(d)$  by  $\sqrt{t_{\text{exp}}}$ .

The rescaled FP distance uncertainties as a function of  $t_{\text{exp}}$  are shown by the dashed black line in Fig. 14a. The coloured regions represent the breakdown of the total uncertainties into each of the constituent terms, so the upper coloured region coincides with the dashed black line. The uncertainty on the plane parameters increases with increasing  $t_{\text{exp}}$ , due to the decreasing sample size (golden regions in panel a). These uncertainties are dominated by  $u(d)$ . The typical measurement uncertainties instead have the opposite trend (blue regions), and are dominated by  $u(s)$ . As a result of these two opposite trends, the total uncertainty  $u_{3d}(\text{dist})$  has a minimum, at  $t_{\text{exp}} \approx 0.25$  hours. This is slightly shorter than the equivalent exposure time of SDSS (vertical dashed line).

The inconsistent nature of the magenta cross-hatched region, which traces the contribution of  $\sigma_{\text{intr}}$ , requires explanation. In principle, this should be independent of  $t_{\text{exp}}$ ; in practice its variation reflects our inability to reliably estimate the measurement uncertainties: we determine the total observed  $\text{rms}$ , so  $\sigma_{\text{intr}}$  is effectively the part of the  $\text{rms}$  not accounted for by the nominal measurement uncertainties.

Panel b is the same as a, but for the  $I_{\text{age}}$  hyperplane. The total uncertainty  $u_{4d}(\text{dist})$  is traced by the upper envelope of the coloured regions, while the dashed black line is  $u_{3d}(\text{dist})$  from panel a, shown for comparison. We notice immediately that, for  $t_{\text{exp}} \gtrsim t_{\text{SDSS}}$ , we have  $u_{4d}(\text{dist}) < u_{3d}(\text{dist})$ . To our knowledge, this is the first time that the inclusion of stellar-population parameters in the FP has been shown to actually improve it as a distance indicator.

On the other hand, for  $t_{\text{exp}} \lesssim 0.3$  hours,  $u_{4d}(\text{dist}) > u_{3d}(\text{dist})$ , we recover the results of M12 (for 6dFGS,  $\langle \text{SNR} \rangle = 13 \text{ \AA}^{-1}$ , Campbell et al. 2014, so it lies outside the range of Fig. 14a). Looking at the breakdown of the distance uncertainties, we also confirm the explanation provided by M12 as to why, for short  $t_{\text{exp}}$ , the FP is a better distance indicator than the 4-d hyperplane. In this case, the measurement uncertainties on  $I_{\text{age}}$  are too large to compensate the reduction in  $\sigma_{\text{intr}}$ . Furthermore, the term due to  $u(s)$  is also larger than for the FP case (cf. panel a). This is because, even though the measurement uncertainties are the same in the two panels, for the 4-d hyperplane the coefficient of  $u(s)$  in Eq. (9) is larger (1.11 vs 1.25, Fig. 8,

panels **a** and **c**). Similar considerations apply to the *age* and mass-to-light ratio hyperplanes.

Incidentally, Fig. 14 shows that even for data less deep than SDSS, the median distance uncertainty is dominated by intrinsic scatter and measurement uncertainties. For a sample size of 5000 galaxies, the uncertainties on the FP parameters (golden shaded regions) are already negligible in the total budget. This means that increasing the sample size does not decrease the median distance uncertainties.

The last two panels of Fig. 14, panels **c** and **d**, repeat panels **a** and **b** respectively, but for a survey of fixed sample size. Compared to the survey of fixed total time, we simply removed the scaling by  $\sqrt{t_{\text{exp}}}$  of the uncertainty in the distance parameters. The results are qualitatively very similar to the previous case.

#### 6.4 Implications for cosmology

In Fig. 15a we show again the median distance uncertainty for a survey of fixed total time, as a function of  $t_{\text{exp}}$ . The solid grey line is  $u_{3d}(\text{dist})$ , the dashed blue line is the  $u_{4d}(\text{dist})$  for the *age* hyperplane, the dash-dotted golden line is for the  $I_{\text{age}}$  hyperplane, and the dotted red line is for the mass-to-light ratio hyperplane. Here we show the uncertainties in their natural units of dex. As expected from the *rms* (Fig. 10a), for sufficiently long  $t_{\text{exp}}$  all three hyperplanes are more precise than the FP. Compared to Fig. 10a, we can see both  $u_{3d}(\text{dist})$  and  $u_{4d}(\text{dist})$  increasing again for the longest  $t_{\text{exp}}$ , as the smaller sample size negatively offsets the gain due to lower  $\sigma_{\text{intr}}$ .

Equality between  $u_{3d}(\text{dist})$  and  $u_{4d}(\text{dist})$  is reached first for the  $\Upsilon_*$  hyperplane, followed by the  $I_{\text{age}}$  and *age* hyperplanes. By happenstance, equality is reached for  $I_{\text{age}}$  at an exposure time equivalent to SDSS (vertical dashed line).

The  $\Upsilon_*$  hyperplane has the highest  $u_{4d}(\text{dist})$ , despite using the observable that is most closely related to the physical formulation of the virial plane (cf. DE21, their eq. 2), (possibly due to large measurement uncertainties, § 6.1). Moreover,  $\Upsilon_*$  shares all the drawbacks of *age* (e.g., the systematics inherent to its measurement; see the discussion for *age* in § 2.6), but none of the benefits. Overall, the  $\Upsilon_*$  hyperplane is the worst of the three candidate replacements for the FP.

The other two implementations, the *age* and  $I_{\text{age}}$  hyperplanes, have substantially lower  $u_{4d}(\text{dist})$ , and are comparable to one another. Both of them use a distance-independent observable as the third independent variable, but  $I_{\text{age}}$  has the critical advantage of being an empirical observable, measurable directly from the spectra without any additional assumptions (cf. § 2.6). Even though  $I_{\text{age}}$  varies with distance (at least due to passive evolution), the same is true for surface brightness; to the extent we use models to correct the latter, we can apply the same models to correct  $I_{\text{age}}$  too. These advantages make the  $I_{\text{age}}$  hyperplane a convincing candidate as an improved distance indicator for cosmology.

Quantitatively,  $I_{\text{age}}$  gives a decrease in the distance uncertainty compared to  $u_{3d}(\text{dist})$  of  $\approx 0.01$  dex. In relative terms, this corresponds to 10 per cent of the FP uncertainty, as shown in Fig. 15b, where the lines display the relative difference between the distance uncertainties from Fig. 15a and  $u_{3d}(\text{dist})$ . The maximum improvement we find is 14 per cent.

For cosmology, this translates into an equal improvement of the measurement uncertainties, for example, on the growth rate of cosmic structures ( $f\sigma_8$ , Fig. 16). We used the Fisher matrix method of Howlett et al. (2017) to forecast the constraints on the growth rate of cosmic structure  $f\sigma_8$ . For this analysis we used the number density from the ongoing Dark Energy Spectroscopic Instrument (DESI; Abareshi et al. 2022) as an example. The number densities for the DESI Bright Galaxy Survey (BGS) and for the DESI pv are from Hahn et al. (2022) and Saulder et al. (2022) respectively. Although DESI pv uses both FP and Tully-Fisher for their forecasts, here we use only the number density for the FP galaxies only (see Fig. 11 in Saulder et al. 2022).

Our Fisher forecasts are plotted in Figure 16. As expected, using the  $I_{\text{age}}$  reduces the uncertainty on  $f\sigma_8$  by 7, 8, and 4 per cent for the first three redshift bins, respectively, compared to the FP. The improvement vanishes as we go to higher redshift as most of the constraining power at high redshift is coming from the BGS survey and not from the pv survey. However, for a lower redshift survey such as SDSS pv survey (Said et al. 2020) of 8,000 galaxies the reduction of  $f\sigma_8$  uncertainty can reach 14 per cent. Compared to SDSS, this proposed survey would have roughly  $1.5\times$  the SNR so  $3\times$  longer  $t_{\text{exp}}$ . In the regime where sample size is important (i.e., where the golden regions of Fig. 14 are non-negligible), it is better to trade  $t_{\text{exp}}$  for sample size. However, when the improvement due to increasing sample size saturates, longer  $t_{\text{exp}}$  can still yield a modest improvement to the inferred distances — and comes with smaller environment bias too.

However, applying the  $I_{\text{age}}$  hyperplane to SDSS data from (H22, Fig. 13b), we find that the residual correlations between the residuals of the  $I_{\text{age}}$  hyperplane and environment are only marginally smaller than the residuals of the FP (Fig. 13, panels **c** and **d**). This reason for the different behaviour between the  $I_{\text{age}}$  hyperplanes of SAMI and SDSS is unclear, though we stress that the two dataset have different measurements of environment ( $\Sigma_5$  for SAMI,  $N_{\text{group}}$  for SDSS). So it appears that — with the current depth of SDSS — there is little improvement to be gained from replacing the FP with the  $I_{\text{age}}$  hyperplane.

However, the residuals of the *age* hyperplane do not correlate with environment, even when using the SDSS sample and  $N_{\text{group}}$  (Fig. 13f). Thus increasing  $t_{\text{exp}}$  enough to overcome the measurement uncertainties on *age* provides a distance indicator that is both more precise and accurate than the FP. This is possible already with the proposed survey with  $t_{\text{exp}} \approx 3 \times t_{\text{SDSS}}$ .

## 7 SUMMARY AND CONCLUSIONS

In this work, we derive a 4-d scaling relation for early-type galaxies, by adding an age-related stellar population observable to the 3-d Fundamental Plane (FP). We considered three of these observables: light-weighted stellar population *age*, *r*–band mass-to-light ratio  $\Upsilon_*$ , and a new empirical index  $I_{\text{age}}$ , obtained as a linear combination of Lick indices (§ 2.6). Crucially, these observables are independent of distance, so the new relations can be used as distance indicators for near-field cosmology. We used a sample of 703 early-type galaxies (selected as closely as possible to the selection criteria from cosmological FP surveys) and utilised

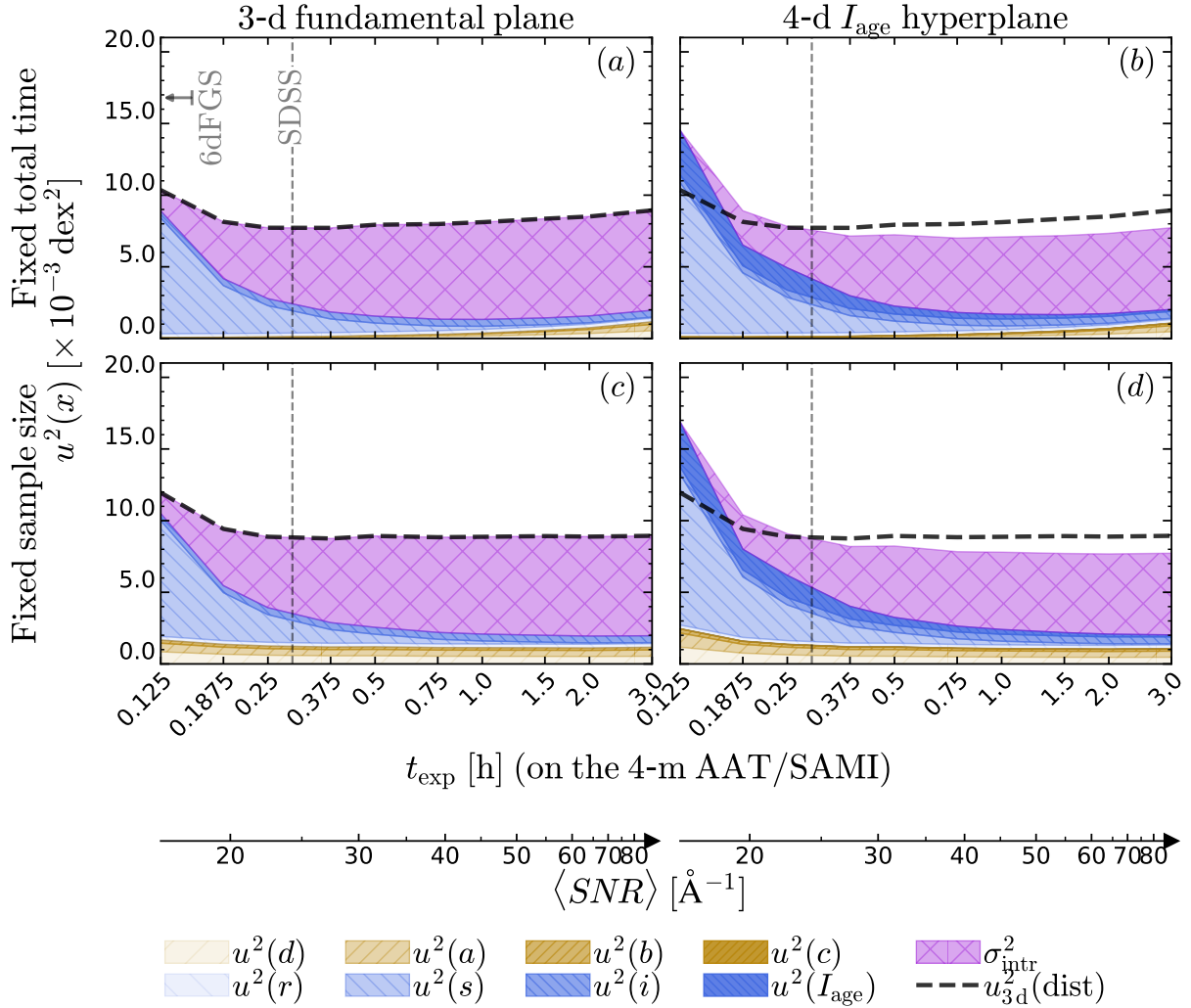


**Figure 14.** Breakdown of the median distance uncertainty as a function of integration time  $t_{\text{exp}}$  (and  $\langle \text{SNR} \rangle$ ). The vertical dashed line is the equivalent exposure time of SDSS; 6dFGS lies outside the range of the figure (grey arrow). We show the median distance uncertainty inferred from the 3-d FP (left column) and from the 4-d  $I_{\text{age}}$  hyperplane (right column). The top row shows the results for a survey of fixed total time; in this case, the sample size is set to 5000 for  $t_{\text{exp}} = 3$  hours, and increases with decreasing  $t_{\text{exp}}$ . The bottom row shows the results for a survey of fixed sample size equal to 5000 for all  $t_{\text{exp}}$ . The golden regions (from  $u^2(d)$  to  $u^2(c)$ ) represent the contribution of the uncertainties about the best-fit parameters; the blue regions (from  $u^2(r)$  to  $u^2(I_{\text{age}})$ ) represent the contribution of the measurement uncertainties; the purple region on top represents the contribution from  $\sigma_{\text{intr}}$ . For both large sample size and high measurement precision,  $\sigma_{\text{intr}}$  dominates the uncertainty budget. The 4-d hyperplane trades lower  $\sigma_{\text{intr}}$  for higher  $u^2(c)$  and, especially,  $u^2(I_{\text{age}})$ , the uncertainty in  $I_{\text{age}}$ . The total uncertainty as a function of  $t_{\text{exp}}$  is traced by the upper envelope; for the 3-d case, the upper envelope is also traced by a thick dashed line, which we replot for direct comparison in the 4-d case. In panels **b** and **d**, whenever the 4-d uncertainty envelope is lower than the thick dashed line, the 4-d approach is better than the 3-d approach.

the large collecting area and long integration times of the SAMI Galaxy Survey on the 4-metre AAT Telescope to find the best tradeoff between long exposure time  $t_{\text{exp}}$  and large sample size that minimises the median distance uncertainty for the new relations. Our conclusions are:

- For the FP, the best-fit coefficients depend on the  $\text{SNR}$  of the data (Fig. 9); the dependence is strong (20 per cent) for short  $t_{\text{exp}}$ , but disappears for  $t_{\text{exp}} > t_{\text{SDSS}}$  (here  $t_{\text{SDSS}} = 0.3$  hours is the exposure time equivalent to that of the SDSS survey). For the hyperplanes, the dependency on  $\text{SNR}$  vanishes only for  $t_{\text{exp}} > 2 \times t_{\text{SDSS}}$ .
- The  $\text{age}$  hyperplane has smaller  $\text{rms}$  than the FP for  $t_{\text{exp}} > 0.5$  hours (Fig. 10a); the minimum  $\text{rms}$  is 0.078 dex

(compared to 0.088 dex for the FP). At the same time, unlike the FP residuals, the hyperplane residuals  $\Delta r$  do not correlate with  $\text{age}$  (Fig. 10b). This is evidence for  $\text{age}$  information going to reduce the  $\text{rms}$  compared to the FP.

- The  $\Upsilon_*$  hyperplane has smaller  $\text{rms}$  than the FP already for  $t_{\text{exp}} > 0.3$  hours (Fig. 10a); the minimum  $\text{rms}$  is 0.082 dex (Fig. 10b), making this the worst of the three hyperplanes. This disappointing performance may be due to the observational uncertainties on  $\Upsilon_*$  being larger than we report (we find 0.05 dex from repeat observations, but require at least 0.08 dex to explain the  $\text{rms}$  of this hyperplane).

- The  $I_{\text{age}}$  hyperplane has  $\text{rms}$  equal to the FP for  $t_{\text{exp}} \approx t_{\text{SDSS}}$  — a prediction we verify using SDSS data (§ 5). For

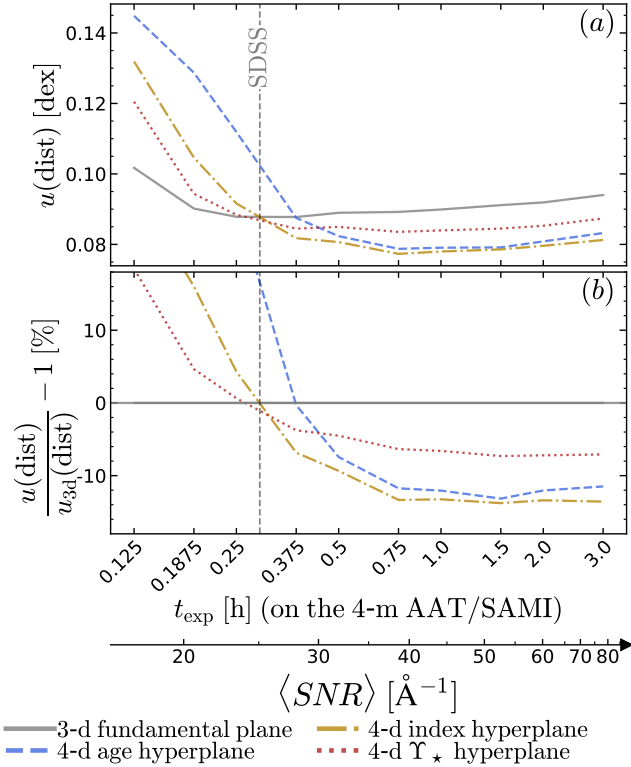


**Figure 15.** Panel **a**: median distance uncertainty as a function of exposure time, comparing the FP (solid grey line), to the three hyperplanes: the age hyperplane (dashed blue line), the  $I_{\text{age}}$  hyperplane (dash-dotted golden line), and the mass-to-light-ratio hyperplane (dotted red line). Panel **b**: same as panel **a**, but the median distance uncertainties are relative to the value from the FP. For spectroscopy with depth comparable to SDSS (vertical dashed line), the  $I_{\text{age}}$  hyperplane is as good a distance indicator as the FP; for longer exposure times, the hyperplane gives a median uncertainty that is about 10 per cent better.

longer  $t_{\text{exp}}$ , the hyperplane outperforms the FP, reaching a minimum  $rms$  of 0.077 (Fig. 10a). For this hyperplane  $\Delta r$  still anticorrelates with  $age$  (although the correlation is weaker and less significant than for the FP; Fig. 10b). This suggests that the  $I_{\text{age}}$  hyperplane uses in part information other than  $age$  to reduce the  $rms$ .

- For the  $I_{\text{age}}$  hyperplane  $\Delta r$  shows only a marginal correlation with environment  $\Sigma_5$  (2- $\sigma$ ), but unlike for the FP, where this correlation is highly significant (Fig. 11). So the hyperplane removes the known environment bias of the FP.

- Using SDSS data and measuring environment with  $N_{\text{group}}$ , we confirm that the  $I_{\text{age}}$  hyperplane reduces the correlation between the residuals and environment, though the correlation is still significant (Fig. 13d). In contrast, the residuals of the  $age$  hyperplane do not correlate with environment (Fig. 13f).

- A partial correlation coefficient analysis shows that, comparing  $age$  and  $\Sigma_5$  (or  $N_{\text{group}}$ ), the residuals of the FP correlate *independently* with both  $age$  and  $\Sigma_5$  (or  $N_{\text{group}}$ ), but the correlation with  $age$  has by far the largest correlation coefficient and highest statistical significance (Fig. 12 and § 5.1) This explains why the  $I_{\text{age}}$  and  $age$  hyperplanes,

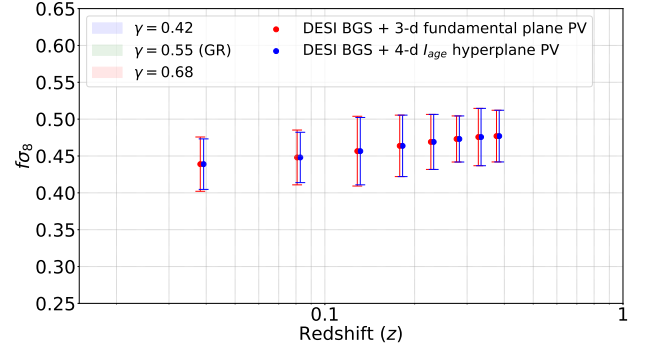


**Figure 16.** Cosmological Fisher forecasts for the growth rate of structure  $f\sigma_8$  from ongoing DESI Bright Galaxy Survey (BGS) and DESI peculiar velocity survey compared to the same survey but using the 4-d hyperplane instead of the 3-d fundamental plane for peculiar velocity. The proposed survey with the  $I_{\text{age}}$  hyperplane would yield 7, 8, and 4 per cent smaller uncertainties (blue circles) than the 3-d FP for the first three redshift bins. There is no improvements for the higher redshift bins as most of the constraining power at high redshift are coming from the BGS survey and not from the pv survey. The different bands show the expected growth rate of structures from GR (green band) and for alternative theories of gravity (blue and red bands).

in correcting the  $age$  bias, reduce ( $I_{\text{age}}$ ) or remove ( $age$ ) the environment bias of the FP.

- When simulating a survey of fixed total time, we find that the median uncertainty for distances derived from the  $I_{\text{age}}$  hyperplane is lower than for the FP for exposure times  $t_{\text{exp}} > 0.3$  hours. This result is confirmed by repeating our experiment with data from SDSS (§ 5).

- Compared to the FP, the median distance uncertainty of the  $I_{\text{age}}$  hyperplane is up to  $\approx 10$  per cent smaller for SNRs larger than those of SDSS.

- Given that  $I_{\text{age}}$  is a distance- and model-independent quantity, the corresponding 4-d hyperplane is a potentially superior substitute for the FP as a distance indicator for low-redshift cosmology.

## ACKNOWLEDGMENTS

We thank the anonymous referee for their insightful comments which greatly improved this article. FDE and AvdW acknowledge funding through the H2020 ERC Consolidator Grant 683184. FDE and RM acknowledge support by the Science and Technology Facilities Council (STFC), by the ERC through Advanced Grant 695671 ‘‘QUENCH’’, and by the UKRI Frontier Research grant RISEandFALL. FDE also acknowledges invaluable help from Brian Van Den Noortgaete. RM also acknowledges funding from a research professorship from the Royal Society. KS acknowledges support from the Australian Government through the Australian Research Council’s Laureate Fellowship funding scheme (project FL180100168).

The SAMI Galaxy Survey is based on observations made at the Anglo-Australian Telescope. The Sydney-AAO Multi-object Integral-field spectrograph (SAMI) was developed jointly by the University of Sydney and the Australian Astronomical Observatory, and funded by ARC grants FF0776384 (Bland-Hawthorn) and LE130100198.

The SAMI input catalogue is based on data taken from the Sloan Digital Sky Survey, the GAMA Survey and the VST ATLAS Survey. The SAMI Galaxy Survey was funded by the Australian Research Council Centre of Excellence for All-sky Astrophysics (CAASTRO), through project number CE110001020, and other participating institutions. The SAMI Galaxy Survey website is <http://sami-survey.org/>.

Funding for SDSS-III has been provided by the Alfred P. Sloan Foundation, the Participating Institutions, the National Science Foundation, and the U.S. Department of Energy Office of Science. The SDSS-III web site is <http://www.sdss3.org/>.

GAMA is a joint European-Australian project based on a spectroscopic campaign using the Anglo-Australian Telescope. The GAMA input catalogue is based on data taken from the Sloan Digital Sky Survey and the UKIRT Infrared Deep Sky Survey. Complementary imaging of the GAMA regions is being obtained by a number of independent survey programmes including GALEX MIS, VST KiDS, VISTA VIKING, WISE, Herschel-ATLAS, GMRT and ASKAP providing UV to radio coverage. GAMA is funded by the STFC (UK), the ARC (Australia), the AAO, and the participating institutions. The GAMA website is <http://www.gama-survey.org/>.

This work is based in part on observations made with ESO Telescopes at the La Silla Paranal Observatory under programme ID 179.A-2004.

This work made extensive use of the freely available [Debian GNU/Linux](#) operative system. We used the [Python](#) programming language ([van Rossum 1995](#)), maintained and distributed by the Python Software Foundation. We made direct use of Python packages [ASTROPY](#) ([Astropy Collaboration et al. 2013](#)), [CORNER](#) ([Foreman-Mackey 2016](#)), [LOESS](#) ([Cappellari et al. 2013b](#)), [LTSFIT](#) ([Cappellari et al. 2013a](#)), [MATPLOTLIB](#) ([Hunter 2007](#)), [MGEFIT](#) ([Cappellari 2002](#)), [NUMPY](#) ([Harris et al. 2020](#)), [PATHOS](#) ([McKerns et al. 2011](#)), [PINGOUIN](#) ([Vallat 2018](#)), [PPXF](#) ([Cappellari & Emsellem 2004](#); [Cappellari 2017, 2022](#)), and [SCIPY](#) ([Jones et al. 2001](#)). The 4-d hyperplane fits used a modified version of the proprietary [LTSFIT](#) algorithm; this modified version is available only for internal use, but may be obtained through a reasonable request to both the [corresponding author](#), and the [original developer](#). All computationally intensive calculations were performed using [DOCKER](#) ([Merkel 2014](#)) and [HTCONDOR](#) ([Thain et al. 2005](#)).

## DATA AVAILABILITY

The data used in this work is publicly available through the [SAMI Data Release 3](#) ([Croom et al. 2021](#)). Ancillary data is from the [GAMA Data Release 3](#) ([Baldry et al. 2018](#)) and raw data is from [SDSS DR7](#) ([Abazajian et al. 2009](#)), [SDSS DR9](#) ([Ahn et al. 2012](#)) and [VST](#) ([Shanks et al. 2013, 2015](#)). The SDSS peculiar velocity sample from ([H22](#)) is available through [Zenodo](#). Age, mass-to-light ratio and  $I_{\text{age}}$  measurements are available by [contacting the corresponding author](#).

## REFERENCES

- Abareshi B., et al., 2022, *AJ*, **164**, 207  
 Abazajian K. N., et al., 2009, *ApJS*, **182**, 543  
 Abolfathi B., et al., 2018, *ApJS*, **235**, 42  
 Ahn C. P., et al., 2012, *ApJS*, **203**, 21  
 Allen J. T., et al., 2015, *MNRAS*, **446**, 1567  
 Astropy Collaboration et al., 2013, *A&A*, **558**, A33  
 Bait O., Barway S., Wadadekar Y., 2017, *MNRAS*, **471**, 2687  
 Baker W. M., Maiolino R., Bluck A. F. L., Lin L., Ellison S. L., Belfiore F., Pan H.-A., Thorp M., 2022, *MNRAS*, **510**, 3622  
 Baldry I. K., et al., 2018, *MNRAS*, **474**, 3875  
 Barone T. M., et al., 2018, *ApJ*, **856**, 64  
 Bernardi M., Domínguez Sánchez H., Margalef-Bentabol B., Nikakhtar F., Sheth R. K., 2020, *MNRAS*, **494**, 5148  
 Bland-Hawthorn J., et al., 2011, *Optics Express*, **19**, 2649  
 Blanton M. R., Roweis S., 2007, *AJ*, **133**, 734  
 Bluck A. F. L., et al., 2019, *MNRAS*, **485**, 666  
 Bluck A. F. L., Maiolino R., Sánchez S. F., Ellison S. L., Thorp M. D., Piotrowska J. M., Teimoorinia H., Bundy K. A., 2020, *MNRAS*, **492**, 96  
 Brough S., et al., 2017, *ApJ*, **844**, 59  
 Bryant J. J., Bland-Hawthorn J., Fogarty L. M. R., Lawrence J. S., Croom S. M., 2014, *MNRAS*, **438**, 869  
 Bryant J. J., et al., 2015, *MNRAS*, **447**, 2857  
 Bundy K., et al., 2015, *ApJ*, **798**, 7  
 Burak Dogruel M., et al., 2024, *arXiv e-prints*, p. [arXiv:2405.10866](#)  
 Campbell L. A., et al., 2014, *MNRAS*, **443**, 1231  
 Cappellari M., 2002, *MNRAS*, **333**, 400  
 Cappellari M., 2017, *MNRAS*, **466**, 798  
 Cappellari M., 2022, *arXiv e-prints*, p. [arXiv:2208.14974](#)  
 Cappellari M., Emsellem E., 2004, *PASP*, **116**, 138  
 Cappellari M., et al., 2013a, *MNRAS*, **432**, 1709  
 Cappellari M., et al., 2013b, *MNRAS*, **432**, 1862  
 Chabrier G., 2003, *PASP*, **115**, 763  
 Chilingarian I. V., Melchior A.-L., Zolotukhin I. Y., 2010, *MNRAS*, **405**, 1409  
 Choi J., Dotter A., Conroy C., Cantiello M., Paxton B., Johnson B. D., 2016, *ApJ*, **823**, 102  
 Cleveland W. S., Devlin S. J., 1988, *Journal of the American Statistical Association*, **83**, 596  
 Colless M., Saglia R. P., Burstein D., Davies R. L., McMahan R. K., Wegner G., 2001, *MNRAS*, **321**, 277  
 Conroy C., Naidu R. P., Zaritsky D., Bonaca A., Cargile P., Johnson B. D., Caldwell N., 2019, *ApJ*, **887**, 237  
 Cortese L., et al., 2016, *MNRAS*, **463**, 170  
 Croom S. M., et al., 2012, *MNRAS*, **421**, 872  
 Croom S. M., et al., 2021, *MNRAS*, **505**, 991  
 Croom S. M., et al., 2024, *MNRAS*, **529**, 3446  
 D'Eugenio F., et al., 2021, *MNRAS*, **504**, 5098  
 D'Onofrio M., et al., 2008, *ApJ*, **685**, 875  
 Davis T. A., et al., 2022, *MNRAS*, **512**, 1522  
 Djorgovski S., Davis M., 1987, *ApJ*, **313**, 59  
 Dogruel M. B., Taylor E. N., Cluver M., D'Eugenio F., de Graaff A., Colless M., Sonnenfeld A., 2023, *ApJ*, **953**, 45  
 Dressler A., Lynden-Bell D., Burstein D., Davies R. L., Faber S. M., Terlevich R., Wegner G., 1987, *ApJ*, **313**, 42  
 Eftekhari F. S., et al., 2022, *MNRAS*, **517**, 4714  
 Emsellem E., Monnet G., Bacon R., 1994, *A&A*, **285**, 723  
 Emsellem E., et al., 2011, *MNRAS*, **414**, 888  
 Faber S. M., Dressler A., Davies R. L., Burstein D., Lynden Bell D., Terlevich R., Wegner G., 1987, in Faber S. M., ed., *Nearly Normal Galaxies. From the Planck Time to the Present*. p. 175  
 Falcón-Barroso J., Sánchez-Blázquez P., Vazdekis A., Ricciardelli E., Cardiel N., Cenarro A. J., Gorgas J., Peletier R. F., 2011, *A&A*, **532**, A95  
 Ferri F., Pudil P., Hatef M., Kittler J., 1994, in GELSEMA E. S.,

- KANAL L. S., eds, Machine Intelligence and Pattern Recognition, Vol. 16, Pattern Recognition in Practice IV. North-Holland, pp 403–413, doi:<https://doi.org/10.1016/B978-0-444-81892-8.50040-7>, <https://www.sciencedirect.com/science/article/pii/B9780444818928500407>
- Forbes D. A., Ponman T. J., Brown R. J. N., 1998, *ApJ*, **508**, L43
- Foreman-Mackey D., 2016, *The Journal of Open Source Software*, **1**, 24
- Gallazzi A., Bell E. F., 2009, *ApJS*, **185**, 253
- Gallazzi A., Charlot S., Brinchmann J., White S. D. M., Tremonti C. A., 2005, *MNRAS*, **362**, 41
- Gargiulo A., et al., 2009, *MNRAS*, **397**, 75
- Graves G. J., Faber S. M., 2010, *ApJ*, **717**, 803
- Graves G. J., Faber S. M., Schiavon R. P., 2009, *ApJ*, **693**, 486
- Green A. W., et al., 2018, *MNRAS*, **475**, 716
- Gregg M. D., 1992, *ApJ*, **384**, 43
- Guzman R., Lucey J. R., 1993, *MNRAS*, **263**, L47
- Hahn C., et al., 2022, arXiv e-prints, p. [arXiv:2208.08512](https://arxiv.org/abs/2208.08512)
- Harris C. R., et al., 2020, *Nature*, **585**, 357
- Howlett C., Staveley-Smith L., Blake C., 2017, *MNRAS*, **464**, 2517
- Howlett C., Said K., Lucey J. R., Colless M., Qin F., Lai Y., Tully R. B., Davis T. M., 2022, arXiv e-prints, p. [arXiv:2201.03112](https://arxiv.org/abs/2201.03112)
- Hudson M. J., Lucey J. R., Smith R. J., Steel J., 1997, *MNRAS*, **291**, 488
- Hudson M. J., Smith R. J., Lucey J. R., Schlegel D. J., Davies R. L., 1999, *ApJ*, **512**, L79
- Hunter J. D., 2007, *Computing in Science and Engineering*, **9**, 90
- Hyde J. B., Bernardi M., 2009, *MNRAS*, **396**, 1171
- Johnson A., et al., 2014, *MNRAS*, **444**, 3926
- Jones E., Oliphant T., Peterson P., et al., 2001, SciPy: Open source scientific tools for Python, <http://www.scipy.org/>
- Jones D. H., et al., 2004, *MNRAS*, **355**, 747
- Jørgensen I., Franx M., Kjaergaard P., 1996, *MNRAS*, **280**, 167
- Liu Y., 2020, *MNRAS*, **497**, 3011
- Magoulas C., et al., 2012, *MNRAS*, **427**, 245
- McDermid R. M., et al., 2015, *MNRAS*, **448**, 3484
- McKerns M. M., Strand L., Sullivan T., Fang A., Aivazis M. A. G., 2011, in Proceedings of the 10th Python in Science Conference. ([arXiv:1202.1056](https://arxiv.org/abs/1202.1056))
- Merkel D., 2014, *Linux journal*, 2014, 2
- Oke J. B., Gunn J. E., 1983, *ApJ*, **266**, 713
- Owers M. S., et al., 2019, *ApJ*, **873**, 52
- Pietrinferni A., Cassisi S., Salaris M., Castelli F., 2004, *ApJ*, **612**, 168
- Pietrinferni A., Cassisi S., Salaris M., Castelli F., 2006, *ApJ*, **642**, 797
- Prugniel P., Simien F., 1996, *A&A*, **309**, 749
- Prugniel P., Simien F., 1997, *A&A*, **321**, 111
- Rousseeuw P. J., Driessen K., 2006, *Data Min. Knowl. Discov.*, **12**, 29
- Saglia R. P., Colless M., Burstein D., Davies R. L., McMahan R. K., Wegner G., 2001, *MNRAS*, **324**, 389
- Said K., Colless M., Magoulas C., Lucey J. R., Hudson M. J., 2020, *MNRAS*, **497**, 1275
- Sánchez-Blázquez P., et al., 2006, *MNRAS*, **371**, 703
- Scott N., et al., 2017, *MNRAS*, **472**, 2833
- Scott N., et al., 2018, *MNRAS*, **481**, 2299
- Shanks T., et al., 2013, *The Messenger*, **154**, 38
- Shanks T., et al., 2015, *MNRAS*, **451**, 4238
- Sharp R., et al., 2006, in Society of Photo-Optical Instrumentation Engineers (SPIE) Conference Series. p. 62690G ([arXiv:astro-ph/0606137](https://arxiv.org/abs/astro-ph/0606137)), doi:[10.1117/12.671022](https://doi.org/10.1117/12.671022)
- Sharp R., et al., 2015, *MNRAS*, **446**, 1551
- Springob C. M., et al., 2012, *MNRAS*, **420**, 2773
- Taylor E. N., et al., 2011, *MNRAS*, **418**, 1587
- Tempel E., Tuvikene T., Kipper R., Libeskind N. I., 2017, *A&A*, **602**, A100
- Thain D., Tannenbaum T., Livny M., 2005, *Concurrency - Practice and Experience*, **17**, 323
- Thomas D., Maraston C., Schawinski K., Sarzi M., Silk J., 2010, *MNRAS*, **404**, 1775
- Trager S. C., Faber S. M., Worthey G., González J. J., 2000, *AJ*, **120**, 165
- Vallat R., 2018, *Journal of Open Source Software*, **3**, 1026
- Vaughan S. P., et al., 2022, *MNRAS*, **516**, 2971
- Vazdekis A., Sánchez-Blázquez P., Falcón-Barroso J., Cenarro A. J., Beasley M. A., Cardiel N., Gorgas J., Peletier R. F., 2010, *MNRAS*, **404**, 1639
- Vazdekis A., et al., 2015, *MNRAS*, **449**, 1177
- Watson P. J., et al., 2022a, *MNRAS*, **510**, 1541
- Watson P. J., et al., 2022b, *MNRAS*, **513**, 5076
- Yoon Y., Park C., 2020, *ApJ*, **897**, 121
- Yoon Y., Park C., 2022, *ApJ*, **936**, 22
- York D. G., et al., 2000, *AJ*, **120**, 1579
- Zaritsky D., Gonzalez A. H., Zabludoff A. I., 2006, *ApJ*, **638**, 725
- de Graaff A., et al., 2020, *ApJ*, **903**, L30
- de Graaff A., et al., 2021, *ApJ*, **913**, 103
- de Graaff A., Franx M., Bell E. F., Bezanson R., Schaller M., Schaye J., van der Wel A., 2023, *MNRAS*, **518**, 5376
- van Rossum G., 1995, Technical Report, CS-R9526
- van de Sande J., et al., 2017, *ApJ*, **835**, 104

## APPENDIX A: THE STELLAR-MASS PLANE AND THE COLOUR HYPERPLANE

In § 3.1 we briefly argued that the stellar-mass plane is a viable alternative to the standard FP. This is shown in Fig. A1a, which has the same y-axis as Fig. 8a, for ease of comparison. We use observations with  $t_{\text{exp}} = 1$  h. While there is a nominal reduction in the observed scatter ( $rms = 0.089$  vs 0.088), this is hardly significant; moreover, an accurate comparison is hard due to the presence of a substantial fraction of outliers in the mas plane (these outliers are clipped by the LTSFIT algorithm, and do not contribute to the  $rms$ ). On the other hand, given that  $\Sigma_*$  has larger observational uncertainties than  $i$  (Taylor et al. 2011), the mass plane ends up with a substantial reduction in intrinsic scatter (from  $\sigma_{\text{intr}} = 0.082$  to 0.075), similar to  $\Upsilon_*$  hyperplane (0.073; Fig. 8d). This suggests a more fundamental nature of the stellar-mass plane compared to the FP, in agreement with theoretical results (de Graaff et al. 2023). We note, however, that the stellar-mass plane’s  $\sigma_{\text{intr}}$  is larger than either the  $I_{\text{age}}$  or  $age$  hyperplanes values (0.065 and 0.064, panels b and c). Ultimately, what matters for the precision of a scaling relation as a distance estimator is the relation’s  $rms$ . In this case, the stellar-mass plane is also worse than the  $I_{\text{age}}$  and  $age$  hyperplanes. This suggests that approaches using  $M_*$  may be less precise distance indicators than the  $I_{\text{age}}$  or  $age$  hyperplanes, at least in the SNR regime considered here.

We remark here that our  $M_*$  measurements are a linear combination of  $i$ -band magnitudes and  $g - i$  colour (Taylor et al. 2011; Bryant et al. 2015). To test if the effect of  $g - i$  colour is sufficient or not to reduce the FP scatter, we use  $g - i$  as fourth variable in the hyperplane (Fig. A1b). This approach gives the same  $rms$  as the mass plane, and larger intrinsic scatter ( $\sigma_{\text{intr}} = 0.083$ ), comparable to the FP ( $\sigma_{\text{intr}} = 0.082$ ; Fig. 8a). This result suggest that the observed reduction in scatter between our FP and mass plane is driven primarily by the use of  $i$ -band magnitude, rather than colour. Indeed, both the mass plane and the  $g - i$ -colour hyperplane

display strong and significant trends between the residuals *age* (panels **c** and **d**). This suggests that the stellar-mass plane may not be able to remove the environment bias that comes with the FP (§ 4.1). Because SAMI spectroscopy is limited to *g* and *r*-band, we cannot test if using *i*-band mass-to-light ratios yields a tighter mass plane or  $\Upsilon_*$  hyperplane; this test would require very high SNR spectroscopy in *i* band, such as is provided by MaNGA (Bundy et al. 2015). However, this test is beyond the scope of this article.

Recently, there have been efforts to use the mass plane for cosmology applications (Dogruel et al. 2023; Burak Dogruel et al. 2024); these authors model simultaneously *s*, *i*,  $M_*$  and Sérsic index *n*, finding a reduced intrinsic scatter. In particular, including *n* in their fit is key to reducing the scatter, and possibly plays a similar role as  $I_{\text{age}}$  or *age* in our analysis. However, this reduced scatter does not translate into an equal reduction in the noise on the inferred galaxy distances. Comparing the mass plane to the  $I_{\text{age}}$  or *age* hyperplanes requires considering the balance between  $\sigma_{\text{intr}}$  and sample size; in fact, while the mass plane has worse  $\sigma_{\text{intr}}$ , this could be overcome by increasing the sample size, via including galaxies of all morphological types in the mass plane. Late-type galaxies, however, also tend to increase  $\sigma_{\text{intr}}$ ; therefore, a direct test is necessary to assess the balance between  $\sigma_{\text{intr}}$ , sample size, and morphology.

## APPENDIX B: CONTRIBUTION OF $[\alpha/\text{Fe}]$ TO THE FUNDAMENTAL PLANE SCATTER

The abundance of  $\alpha$ elements relative to iron is known to correlate with the FP residuals (Gargiulo et al. 2009), even though this anti-correlation is weaker (smaller-magnitude correlation coefficient) and less significant than the anti-correlation with *age* (DE21). In our framework, a direct comparison would be unfair, because precise  $[\alpha/\text{Fe}]$  measurements require higher SNR than *age* (Liu 2020). In this section, we compare  $[\alpha/\text{Fe}]$  measurements obtained from the SAMI data (i.e., without degrading the SNR) to *age* measurements from the SAMI mocks with  $t_{\text{exp}} = 1$  hour. The goal is to assess, at least qualitatively, whether *age* and  $[\alpha/\text{Fe}]$  play independent roles in producing the FP residuals.

We use two alternative  $[\alpha/\text{Fe}]$  values: measurements based on Lick indices, taken from the SAMI DR3 (described in Scott et al. 2017, labelled  $[\alpha/\text{Fe}]_{\text{Lick}}$ ), and our own measurements from full spectral fitting, obtained using PPXF (following the methodology of Vazdekis et al. 2015 and Liu 2020; labelled simply  $[\alpha/\text{Fe}]$ ).

The results are shown in Fig. B1, where we show  $[\alpha/\text{Fe}]$  vs *age*, colour-coded by the FP residuals  $\Delta r$ . Panels **a** and **b** show the two different estimates of  $[\alpha/\text{Fe}]$ , which we find to be in excellent agreement. Regardless of how  $[\alpha/\text{Fe}]$  is measured, we find that the FP residuals  $\Delta r$  anti-correlate with both *age* and  $[\alpha/\text{Fe}]$ , with older and  $\alpha$ -element enriched galaxies lying preferentially below the FP. The *age*– $\Delta r$  anti-correlation has a larger-magnitude coefficient and higher statistical significance than the  $[\alpha/\text{Fe}]$ – $\Delta r$  anti-correlation. This is in agreement with DE21, but at variance with Gargiulo et al. (2009), likely due to their smaller sample size and lower data quality. Using partial correlation coefficients, we find that  $\Delta r$  correlates independently with both *age* and  $[\alpha/\text{Fe}]$ , with the *age*– $\Delta r$  correlation coefficient be-

ing roughly twice the  $[\alpha/\text{Fe}]$ – $\Delta r$  correlation coefficient. As we already discussed in DE21, it is still unclear why  $[\alpha/\text{Fe}]$ , which is not associated with strong trends in  $\Upsilon_*$ , correlates with the FP residuals. We discuss this subject in § 6.2.

This paper has been typeset from a  $\text{\TeX}/\text{\LaTeX}$  file prepared by the author.

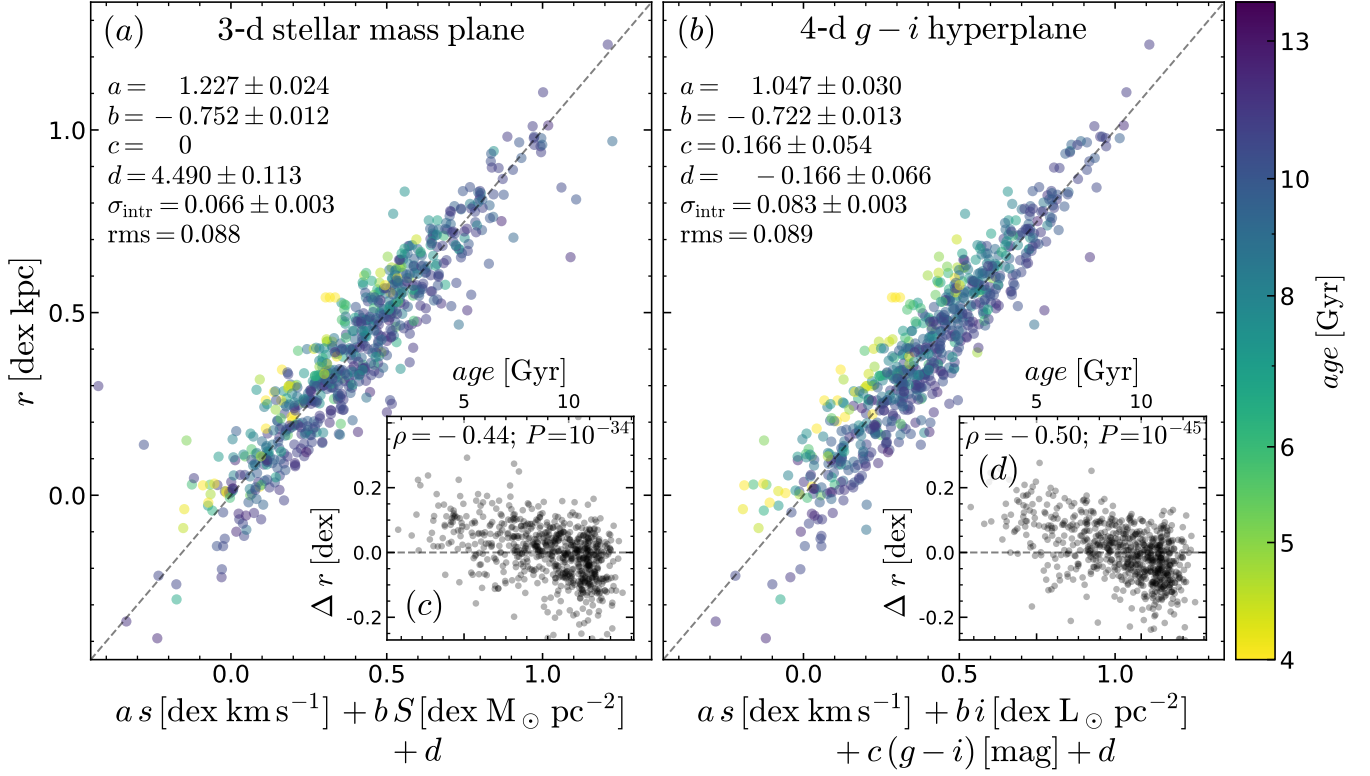


**Figure A1.** Predicted vs measured galaxy size using the stellar-mass surface density (panel a), and the hyperplane where  $g-i$  colour is used as fourth variable (panel b). The stellar-mass plane shows the same rms, but lower  $\sigma_{\text{intr}}$  than the FP (Fig. 8a).

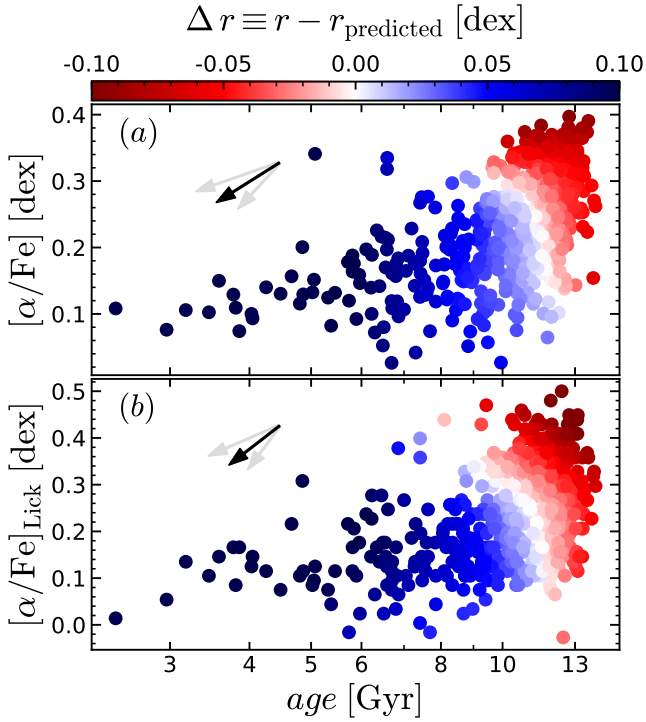


**Figure B1.** Distribution of the residuals of the 3-d FP as a function of both stellar population age and local environment density. The residuals have been LOESS smoothed to highlight the trend. The arrow is a graphical representation of the partial correlation coefficients; it has an angle of  $(217 \pm 14)^\circ$ , with the uncertainties encompassing the 1<sup>st</sup> and 99<sup>th</sup> percentiles. An angle of  $180^\circ$  would correspond to perfect anti-correlation between  $\Delta r$  and *age* and no independent correlation with  $[\alpha/\text{Fe}]$ . Our findings suggest that *age* and  $[\alpha/\text{Fe}]$  have independent roles in driving the residuals  $\Delta r$ , with the *age* correlation coefficient being roughly twice the  $[\alpha/\text{Fe}]$  correlation coefficient. The two panels show two different estimates of  $[\alpha/\text{Fe}]$ , from full spectral fitting (panel a) and from Lick indices (panel b); both give very similar results.